
















Λ CDM not dead yet: massive high- z Balmer break galaxies are less common than previously reported

Guillaume Desprez¹★, Nicholas S. Martis^{1,2}, Yoshihisa Asada^{1,3}, Marcin Sawicki¹†,
Chris J. Willott², Adam Muzzin⁴, Roberto G. Abraham^{5,6}, Maruša Bradač^{7,8}, Gabe Brammer^{9,10},
Vicente Estrada-Carpenter¹, Kartheik G. Iyer¹¹, Jasleen Matharu^{9,10}, Lamiya Mowla¹²,
Gaël Noirot¹, Ghassan T. E. Sarrouh⁴, Victoria Strait^{9,10}, Rachel Gledhill^{9,10}, and Gregor Rihtaršič⁷

¹ Department of Astronomy & Physics and Institute for Computational Astrophysics, Saint Mary's University, 923 Robie Street, Halifax, NS B3H 3C3, Canada

² NRC Herzberg, 5071 West Saanich Rd, Victoria, BC V9E 2E7, Canada

³ Department of Astronomy, Kyoto University, Sakyo-ku, Kyoto 606-8502, Japan

⁴ Department of Physics and Astronomy, York University, 4700 Keele St. Toronto, Ontario, M3J 1P3, Canada

⁵ David A. Dunlap Department of Astronomy and Astrophysics, University of Toronto, 50 St. George Street, Toronto, Ontario, M5S 3H4, Canada

⁶ Dunlap Institute for Astronomy and Astrophysics, 50 St. George Street, Toronto, Ontario, M5S 3H4, Canada

⁷ Department of Mathematics and Physics, Jadranska ulica 19, SI-1000 Ljubljana, Slovenia

⁸ Department of Physics and Astronomy, University of California Davis, 1 Shields Avenue, Davis, CA 95616, USA

⁹ Cosmic Dawn Center (DAWN), Denmark

¹⁰ Niels Bohr Institute, University of Copenhagen, Jagtvej 128, DK-2200 Copenhagen N, Denmark

¹¹ Columbia Astrophysics Laboratory, Columbia University, 550 West 120th Street, New York, NY 10027, USA

¹² Whitin Observatory, Department of Physics and Astronomy, Wellesley College, 106 Central Street, Wellesley, MA 02481, USA

Accepted 2024 April 18. Received 2024 April 10; in original form 2023 September 29

ABSTRACT

Early *JWST* observations that targeted so-called double-break sources (attributed to Lyman and Balmer breaks at $z > 7$), reported a previously unknown population of very massive, evolved high-redshift galaxies. This surprising discovery led to a flurry of attempts to explain these objects' unexpected existence including invoking alternatives to the standard Λ CDM cosmological paradigm. To test these early results, we adopted the same double-break candidate galaxy selection criteria to search for such objects in the *JWST* images of the CANadian NIRISS Unbiased Cluster Survey (CANUCS), and found a sample of 19 sources over five independent CANUCS fields that cover a total effective area of ~ 60 arcmin² at $z \sim 8$. However, (1) our SED fits do not yield exceptionally high stellar masses for our candidates, while (2) spectroscopy of five of the candidates shows that while all five are at high redshifts, their red colours are due to high-EW emission lines in star-forming galaxies rather than Balmer breaks in massive, evolved systems. Additionally, (3) field-to-field variance leads to differences of ~ 1.5 dex in the maximum stellar masses measured in the different fields, suggesting that the early single-field *JWST* observations may have suffered from cosmic variance and/or sample bias. Finally, (4) we show that the presence of even a single massive outlier can dominate conclusions from small samples such as those in early *JWST* observations. In conclusion, we find that the double-break sources in CANUCS are not sufficiently massive or numerous to warrant questioning the standard Λ CDM paradigm.

Key words: galaxies: high-redshift – galaxies: evolution – dark ages, reionization, first stars

1 INTRODUCTION

Observations of the cosmic dawn era are crucial to our comprehension of how the first galaxies form and evolve. In its first year of operation, *JWST* (Gardner et al. 2023) opened a new window on this particular epoch, allowing for the observation of galaxies in a universe just a few 100 Myr old (Curtis-Lake et al. 2023; Robertson et al. 2023; Arrabal Haro et al. 2023; Bunker et al. 2023b; Wang et al. 2023c). Such observations have the potential to expand our knowledge on the Epoch of Reionisation (EoR) and its mechanism

(e.g., Robertson 2022; Atek et al. 2023) as well as to challenge the current paradigm of Λ CDM cosmology.

This is the case with the detection of several massive galaxies at high redshift reported by Labbé et al. (2023b, hereafter L23) in the Cosmic Evolution Early Release Science Survey (CEERS) data (Bagley et al. 2023). These were selected on the basis of a double-break feature in their photometric spectral energy distributions (SED), attributed to the Lyman and Balmer breaks redshifted to $z > 7$. The very high stellar masses reported by L23 for these sources – high in part due to the presence of evolved stellar populations marked by the putative Balmer breaks – disagree with both model predictions (Menci et al. 2022; Boylan-Kolchin 2023; Lovell et al. 2023) and pre-*JWST* observations (Stefanon et al. 2021; La-

★ e-mail: guillaume.desprez@smu.ca

† Canada Research Chair

porte et al. 2023). Their discovery thus spurred a flurry of activity that attempted to explain these objects’ surprising existence by invoking alternatives to the standard Λ CDM cosmological model (Biagetti et al. 2023; Forconi et al. 2023; Hütsi et al. 2023; Lovell et al. 2023; Malekjani et al. 2023; Menci et al. 2022; Su et al. 2023; Wang & Liu 2022; Wang et al. 2023a; Dayal & Giri 2024, and many others).

Since these first results, a number of studies have debated whether *JWST* observations of these and other high redshift galaxies do indicate a tension between Λ CDM and the measured galaxy stellar masses in the early universe. For instance, Xiao et al. (2023) report, in the First Reionization Epoch Spectroscopic Complete Survey (FRESCO, Oesch et al. 2023), the detection of $z > 5$ galaxies whose stellar masses are hard to explain without assuming extreme star-formation efficiencies, at the limit of tension with standard cosmology. Additionally, galaxies with possible photometric redshifts (photo- z) larger than $z = 10$ have been found in the COSMOS-Web survey (Casey et al. 2023b) with estimated stellar masses that require larger than expected star-formation efficiencies (Casey et al. 2023a). On the other hand, Franco et al. (2023) presents a population of $z \geq 9$ sources in the same COSMOS-Web survey, for which the derived masses are not in tension with galaxy formation in Λ CDM. Vikaeus et al. (2024) looked at the strength of Balmer breaks in $z > 6$ galaxy spectra and did not find severe deviation from the predictions of simulations (Mauerhofer & Dayal 2023; Wilkins et al. 2024).

Additionally, some studies have invoked astrophysical reasons why the reported high masses could be overestimated thereby alleviating or eliminating the tension with Λ CDM. For example, while searching for and characterising high- z Balmer-break candidate galaxies in the Prime Extragalactic Areas for Reionization and Lensing Science (PEARLS, Windhorst et al. 2023), Trussler et al. (2023) find that the large stellar masses derived in L23 could be due to the assumptions made in the mass inference, and suggest that the red break in the photometry could be caused by strong emission lines, dusty continuum, and active galactic nuclei (AGN) contributions. Thus an appropriate accounting of these contributions can alleviate the need for an evolved stellar population to fit the Balmer break, leading to stellar masses in better agreement with galaxy formation theory expectations (Lovell et al. 2023). A similar conclusion is reached by Barro et al. (2024) after looking at extremely red objects in CEERS. They find that their sources are well fit whether assuming massive and dusty SEDs or accounting for the contribution of AGN, although they conclude that both scenarios cause problems as either massive galaxies or bright AGN are found to be too numerous at high redshift.

Some sources from the L23 CEERS sample have already been studied further, mitigating the results presented by L23. Two of these sources had spectroscopic follow-up, one being confirmed at redshift $z = 7.9932$ (Fujimoto et al. 2023) with the presence of $H\beta$ and $[OIII]$ emission lines, and the other being identified as an AGN at $z = 5.624$ (Kocevski et al. 2023), thus being inconsistent with the initial assumption of lying at $z > 7$. Also, Endsley et al. (2023b) refit the most massive object from the CEERS double-break sample, but assuming different star formation histories, emission line and AGN contributions to the photometry, leading to lower stellar masses.

However, while the debate in the literature continues, it is important to keep in mind that since high- z galaxy selection methods vary and each is incomplete in some way, a conclusive disagreement of just one of the different selection methods with Λ CDM is sufficient to cause problems for the accepted cosmological paradigm. Put another way, if the type of sources reported in L23 turns out to be both very massive and common, then lack of disagreement between Λ CDM and sources selected by other techniques is moot. To ensure that the tensions with Λ CDM are real, it is thus important to consider

and further test each challenging population. This test is what we aim to do for the double-break sources in order to assess whether their nature as high-mass high- z galaxies holds and thus continues to challenge Λ CDM.

The scope of this work is thus to look for double-break sources similar to those in L23 and to understand if this population is really as numerous and massive as originally reported. We do so using the deep imaging data of the CANadian NIRISS Unbiased Cluster Survey (CANUCS, Willott et al. 2022). CANUCS contains deep *JWST*/NIRCam (Rieke et al. 2023) imaging over 10 fields along 5 widely separated lines-of-sight with total dual filter integration time of 123 hours, covering a total area of ~ 100 arcmin². The combination of imaging depth, multi-wavelength coverage, and independent sightlines makes CANUCS one of the most comprehensive extragalactic NIRCam imaging projects executed in *JWST* Cycle 1. Five of the ten CANUCS fields target strong-lensing cluster cores and are covered as well with *JWST*/NIRISS (Doyon et al. 2023) slitless spectroscopy (Willott et al. 2022) and *JWST*/NIRSpec (Jakobsen et al. 2022) multi-object prism spectroscopy. The other five fields are parallel fields covered with only NIRCam imaging. With its design, the CANUCS survey allows for a control of cosmic and sample variances (field-to-field variance) and gives a representative view of the general galaxy population distributions. It also benefits from deep ancillary *HST*/ACS and *HST*/WFC3 data providing up to 20 band photometry in some fields, thus allowing for tight fits of source SEDs. For all these reasons, CANUCS offers a prime data set to investigate the nature and properties of the bright double-break sources.

Throughout this work, we assume flat Λ CDM cosmology, with $\Omega_\Lambda = 0.7$, $\Omega_m = 0.3$, and $H_0 = 70$ km s⁻¹ Mpc⁻¹. Magnitudes are given in the AB system (Oke & Gunn 1983). We adopt the Chabrier (2003) stellar initial mass function (IMF) in this paper and all results obtained with other IMFs are rescaled to it (Speagle et al. 2014).

2 DATA

We use the data acquired by the CANUCS NIRISS GTO Program #1208 (Willott et al. 2022, DOI) which covers five different strong lensing cluster fields: Abell 370 ($z = 0.375$), MACS J0416.1–2403 (hereafter MACS 0416, $z = 0.395$), MACS J0417.5–1154 (hereafter MACS 0417, $z = 0.443$), MACS J1149.5+2223 (hereafter MACS 1149, $z = 0.543$), and MACS J1423.8+2404 (hereafter MACS 1423, $z = 0.545$) (Soucail 1987; Ebeling et al. 2001). As NIRCam and NIRISS are operated in parallel, each of the five cluster fields is accompanied by a NIRCam flanking field and a NIRISS flanking field.

The cluster fields (denoted *CLU* in Table 1) are covered with the NIRCam F090W, F115W, F150W, F200W, F277W, F356W, F410M, and F444W filters with exposure times of 6.4 ks each. These fields are also covered by NIRISS with both GR150R and GR150C grisms through the F115W, F150W and F200W bands with total exposure 19.2 ks in all three filters.

In the NIRCam flanking fields (denoted *NCF* in Table 1), the medium-band F140M, F162M, F182M, F210M, F250M, F300M, F335M, F360M and F410M filters are used in addition to the broadband F090W, F115W, F150W, F277W, and F444W, with exposure times of 10.3 ks for 10 filters and 5.7 ks for 4 filters.

In all fields, we also use the available *HST* optical and near-IR

¹ CANUCS contains a further 5 fields of NIRISS spectroscopy and limited imaging although these are not used in the present work.

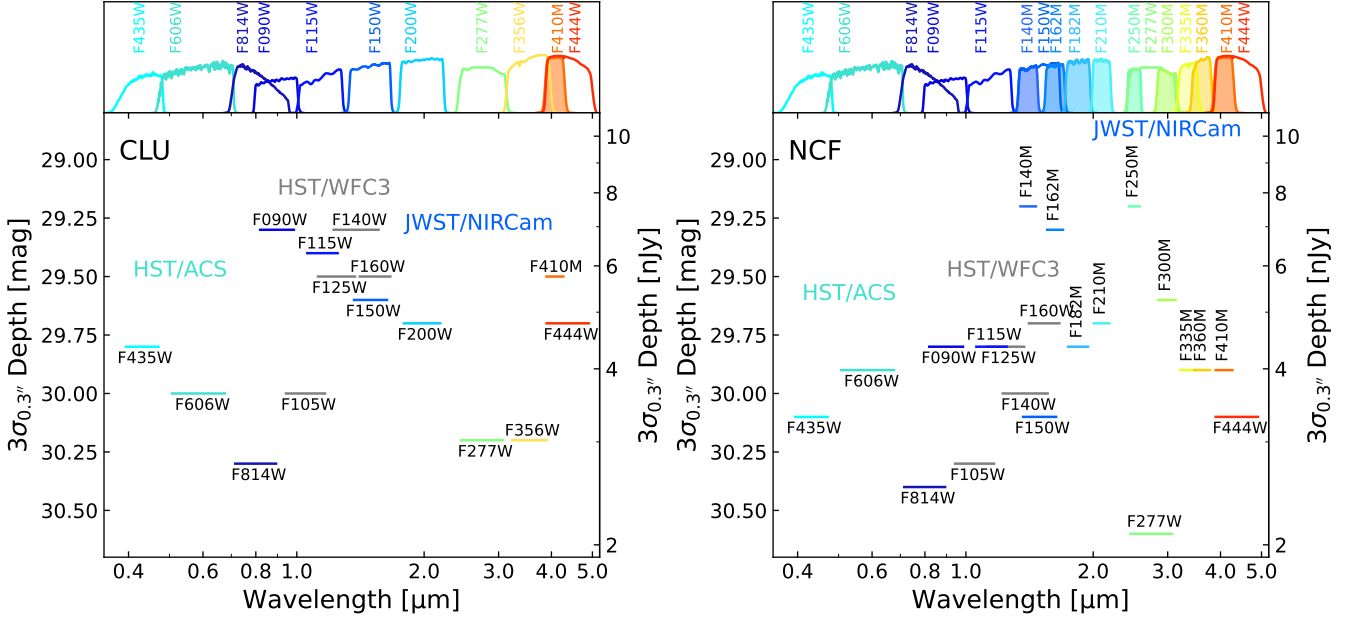


Figure 1. Summary of the median depths (3σ in $0.3''$ apertures) measured across the five different fields in all *HST/ACS* and *JWST/NIRCam* filters observed, split by *CLU* (left panels) and *NCF* pointings (right panels). *HST/WFC3* measurements have been included, however the coverage with these bands is uneven across the different fields, as shown in Table A2.

imaging data. Depending on the field, there is coverage in some of ACS F435W, F606W, F814W, WFC3/UV F438W, F606W, and WFC3/IR F105W, F110W, F125W, F140W, F160W. These data are predominantly from programs HST-GO-11103 PI Ebeling, HST-GO-12009 PI von der Linden, HST-GO-12065 PI Postman, HST-GO-13504 PI Lotz, HST-GO-14096 PI Coe, HST-GO-15117 PI Steinhart and HST-GO-16667 PI Bradač.

NIRSpec spectroscopy has been acquired for four of the five CANUCS clusters at the time of writing, and MACS 1149 spectroscopy is scheduled for December 2023. The spectra are observed using the PRISM/CLEAR disperser and filter, through three Micro-Shutter Assembly (MSA) masks per cluster with total exposure time of 2.9 ks per MSA configuration.

2.1 Imaging

The CANUCS image reduction, calibration and photometry extraction are done in a manner similar to that in Noirot et al. (2023), which is further described in Asada et al. (2024). We provide here a brief description of the main steps of this procedure.

The NIRCam images were processed with the standard STScI *JWST* pipeline and with the Grism redshift & line analysis software (Grizli, Brammer 2023). The *JWST* and *HST* images were drizzled onto a common pixel grid with a scale of 40 milli-arcsec pixel $^{-1}$, using the *Gaia* DR3 astrometry (Gaia Collaboration et al. 2016, 2023).

In the cluster fields, the brightest cluster galaxies (BCGs), as well as other bright foreground galaxies, had their light profiles modeled and subtracted from the images (Martis et al. 2024). These BCG-subtracted images were then convolved with empirically-determined kernels to homogenise their point spread functions (PSFs) to that of the F444W filter.

In all fields, χ_{mean} -detection images (Drlica-Wagner et al. 2018) were constructed by combining all BCG-subtracted non-PSF ho-

Table 1. Summary of the CANUCS fields used in this work. Each field has a unique two-digit Field ID code and all source IDs start with the Field ID code of the field they are in. The number of selected double-break galaxies is given in the Sources [#] column. The sky areas and volumes between $z = 7.0$ – 8.5 quoted in the table account for the lensing magnification assuming a redshift $z = 8$ and area masked by other sources.

Cluster	Field	ID	Sources [#]	Area $z \approx 8$ [arcmin 2]	Volume [10^3 Mpc 3]
MACS 0417	<i>CLU</i>	11	2	$4.57^{+0.47}_{-0.13}$	$13.79^{+1.42}_{-0.37}$
	<i>NCF</i>	12	1	$6.30^{+0.18}_{-0.09}$	$19.01^{+0.48}_{-0.13}$
Abell 370	<i>CLU</i>	21	4	$3.54^{+0.11}_{-0.12}$	$10.77^{+0.25}_{-0.3}$
	<i>NCF</i>	22	1	$6.30^{+0.03}_{-0.05}$	$19.01^{+0.06}_{-0.1}$
MACS 0416	<i>CLU</i>	31	3	$6.05^{+0.05}_{-0.06}$	$18.23^{+0.09}_{-0.13}$
	<i>NCF</i>	32	1	$6.52^{+0.08}_{-0.08}$	$19.65^{+0.02}_{-0.03}$
MACS 1423	<i>CLU</i>	41	2	$5.73^{+0.21}_{-0.15}$	$16.74^{+0.58}_{-0.39}$
	<i>NCF</i>	42	3	$7.38^{+0.06}_{-0.05}$	$22.22^{+0.05}_{-0.04}$
MACS 1149	<i>CLU</i>	51	1	$6.48^{+0.11}_{-0.11}$	$19.56^{+0.19}_{-0.17}$
	<i>NCF</i>	52	1	$7.59^{+0.09}_{-0.09}$	$22.88^{+0.01}_{-0.01}$

mogenised images across all available bands. Source detection and photometry extraction were done using the python photutils package (Bradley et al. 2023). The detection was run on the χ_{mean} -detection image with a "hot-cold" two-mode strategy, and photometry was then measured in all bands using the BCG-subtracted PSF homogenised images, through matched Kron (Kron 1980) and circular apertures of several diameters. In this project we used the $0.3''$ circular diameter photometry in all bands, corrected to total photometry using Kron fluxes in F444W. Flux uncertainties are estimated using empty apertures in noise-normalised images in each band. Figure 1 presents the median 3σ magnitude depths reached in all

bands across the five sight-lines. The detailed information of filter availability and depths for the different fields is quoted in Table A2.

2.2 Spectroscopy

The NIRISS slitless spectroscopy was first processed with `Grizli` (Brammer 2023) and subsequent reduction of the grism data was done as in Noirot et al. (2023) (see also Matharu et al. 2023). The NIRSpec data was processed using the STScI *JWST* pipeline (software version 1.8.4 and `jwst_1030.pmap`) and the `msaexp` package (Brammer 2022). The processing of the raw data is done in a way similar to Withers et al. (2023). We used the standard *JWST* pipeline for the level 1 processing where we obtained the rate fits files from the raw data. We enabled the jump step option `expand_large_events` to mitigate contamination by snowball residuals, and also used a custom persistence correction that masked out pixels which approach saturation within the following 1200 s for any readout groups. We then used `msaexp` to do level 2 processing where we performed the standard wavelength calibration, flat-fielding, path-loss correction, and photometric calibration, and obtained the 2D spectrum for each source. The 1D spectrum was extracted by collapsing the 2D spectrum using an inverse-variance weighted kernel following the prescription by Horne (1986).

2.3 Strong lensing models

The CANUCS survey targets massive cluster fields. Therefore, to measure properly the physical properties of the background sources close to the cluster centres, one must know the magnification due to lensing effects. Strong lensing models are thus needed to assess the magnification produced by the different clusters. We use strong lensing models we built using the code `Lenstool` (Kneib 1993; Jullo et al. 2007). These models leverage previous models constrained with *HST* data as well as the new CANUCS *JWST* data, adding new multiple image systems that we identified as well as new spectroscopic constraints.

For MACS 0417, we update the constraints of the Mahler et al. (2019) and Jauzac et al. (2019) models with new multiple image systems and with new spectroscopic redshifts for previously known ones (e.g., Asada et al. 2023; Strait et al. 2023). The details of the *JWST*-updated model will be presented in Desprez et al. (in prep.). In the case of Abell 370, a model is constructed leveraging the constraints of previous models from the literature (e.g., Strait et al. 2018; Lagattuta et al. 2019, 2022) which are updated and will be presented in Gledhill et al. (in prep.). Rihtaršič et al. (in prep.) will present the update of the Bergamini et al. (2023) model for MACS 0416. The MACS 1423 model uses the constraints presented in Hoag et al. (2017) and will be detailed in Desprez et al. (in prep.). Finally, in the case of MACS 1149, our lensing model uses constraints of Desprez et al. (2018) and all the details will be reported in Rihtaršič et al. (in prep.). All these models include cluster-size and galaxy-size massive halos, described as double Pseudo-Isothermal Elliptical (dPIE) profiles (Elíasdóttir et al. 2007) whose properties are optimised through χ^2 minimisation of the distance between observed multiple images and model predicted ones.

From these models, convergence and shear maps are derived for 100 randomly drawn samples from the optimisation of their parameters, allowing us to account for errors in magnification. The maps created have a size of $20' \times 20'$ centred on the cluster BCGs and a pixel resolution of 600 milli-arcsec pixel^{-1} .

2.4 Area and completeness

To compute the effective area that the CANUCS survey covers at high- z , we need to account for the magnification due to the clusters and any masked area occupied by other sources. This is done by simulating images of galaxies at different random positions in the fields and recovering them with the CANUCS photometry pipeline. Our selection criteria (Section 3.1) require galaxies to have F444W magnitudes < 27 , which corresponds to $S/N > 30$ in this filter for typical high- z galaxies in all the CANUCS fields. Hence there is no incompleteness of the sample due to faint objects not appearing in the detection images. Consequently, we simulate galaxies with flux-density equal to magnitude=28 in all filters. Such galaxies are detected at high S/N in the detection images and are only absent when masked by other sources.

The images of the galaxies presented in L23 are very compact, so we use simulated Sersic profiles with ellipticities distributed normally with a mean of 0.3 and standard deviation $\sigma = 0.2$, Sersic indices distributed normally with a mean of 1.5 and $\sigma = 0.3$, and effective radii with a flat distribution ranging from 0.5 to 0.8 pixels (20 to 32 milli-arcsec). As described previously, the completeness calculations are not sensitive to these details, because both the sample and simulated galaxies are bright enough that they always appear in the detection catalog unless in a region of sky occupied by other galaxies. Simulated galaxies are inserted in the survey images at random positions in $6'' \times 6''$ boxes covering the full images. The data is then processed through the photometry pipeline, allowing us to account for incompleteness in the source detection due to overlap with other sources. The median magnifications and associated 16th and 84th percentile limits are computed for the simulated source positions assuming $z = 8$. The area in which the sources have been placed are then corrected for magnification. The full area of each field is then computed by summing the corrected areas of all simulated sources that are recovered after the pipeline detection. The full process is repeated three times for each field with a different random number seed for the placement of simulated galaxies. The difference between each of the three runs is $\approx 1\%$, showing that further iterations to increase statistics are not required. The effective areas from the three runs are averaged, with uncertainties computed by adding the standard deviation of the three results to the results obtained with the 16th and 84th percentile of magnification in quadrature. The results are quoted in Table 1 for all fields. Volumes are computed between $z = 7.0-8.5$ for all fields, with details also given in Table 1, and add up to a total volume of $185_{-2}^{+3} \times 10^3 \text{ Mpc}^3$ over the full survey.

3 ANALYSIS

In all CANUCS *CLU* and *NCF* fields double-break candidates are selected in a manner similar to L23. The selected sources are then fit to obtain redshifts and stellar mass measurements. Our population of double-break sources are then compared to that reported by L23. The details of this procedure are given in the following sections.

3.1 Selection

We adopt similar selection criteria as those in L23 for the double-break sources. These consist of two colour cuts,

$$\begin{aligned} F150W - F277W &< 0.7, \\ F277W - F444W &> 1.0, \end{aligned}$$

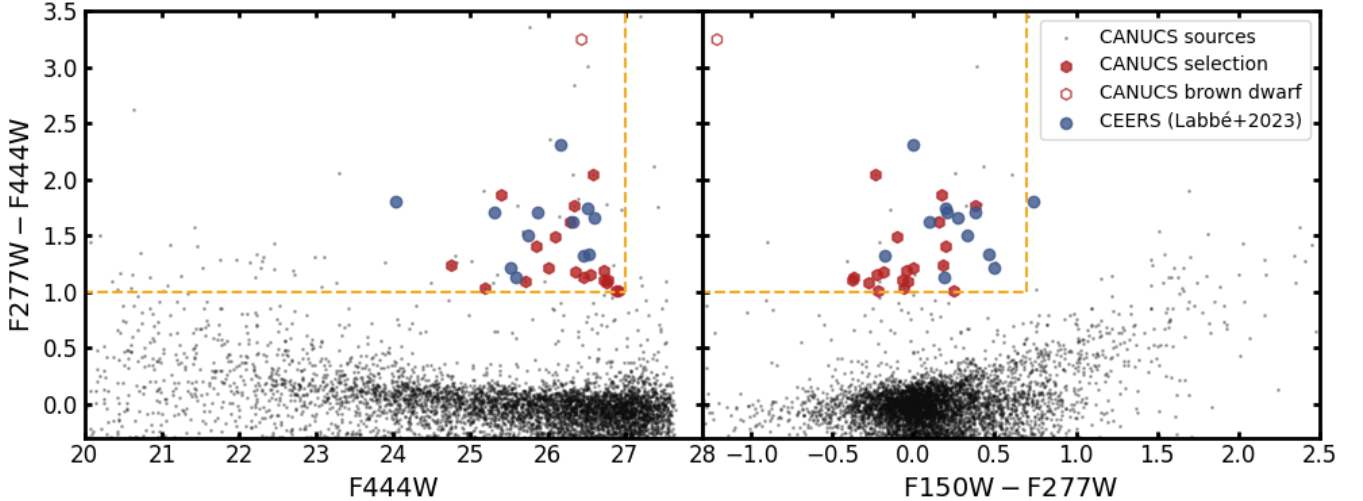


Figure 2. Colour-magnitude and colour-colour diagrams used to select the high- z double-break galaxies. The red hexagons represent the selected sources in the CANUCS data, which are compared to the CEERS (L23) sources shown as blue circles. The dashed lines indicate the cuts that have been applied to the photometric data. The open red hexagon is a CANUCS brown dwarf, easily identified by its extreme colours in the colour-colour diagram.

in addition to two magnitude cuts,

$$F444W < 27,$$

$$F150W < 29.$$

To ensure proper detection of sources, we also imposed a signal-to-noise ratio (S/N) cut in $F444W > 8$. Finally, in the F090W band as well as in all the available *HST* optical bands non-detections were defined as sources with $S/N < 2$ in order to ensure a selection of high- z sources. We note that the S/N criterion on the F090W band makes our sample less likely to include $z \sim 7$ sources compared to the CEERS sample that does not possess this band. The colour and magnitude cuts are illustrated in Fig. 2. We point out that the magnitudes presented are not corrected for lensing, but most sources have estimated magnifications of $\mu < 2$, which leads to, at most, a $F444W$ magnitude larger by 0.75 mag. All the selected sources are then visually inspected to avoid any contamination by noise, bad pixels, light from nearby objects, or possible confusion with lower-redshift interlopers. The candidate cutouts and their photometry are shown in Figs. 4, A1, A2, A3, and A4. After these steps, our selection contains 20 double-break candidates, of which one is discarded due to discrepant colours compared to the bulk of the sample (see Fig. 2), a point-like appearance in all filters, and an SED that is consistent with that of a cool brown dwarf (see Fig A1). This leaves us with a sample of 19 double-break candidates.²

The distribution of the candidates over the different fields is reported in Table 1. We note variation in the number of candidates from cluster to cluster, with five sources for Abell 370 and MACS 1423 but only two for MACS 1149. If we make the comparison field to field, the largest concentration of sources is found in the Abell 370 cluster field with four sources, with five fields containing only one double-break candidate each.

Figure 2 shows the position of all selected sources in colour-magnitude and colour-colour plots. It also presents the L23 candi-

dates, with photometry taken from that paper. Considering the low values of cluster magnification for most of our candidates (see Table A1), most of our sources are intrinsically bright, which means that we are probing the same population of sources as did L23, even if we do not see any source as bright as the brightest L23 object.

Finally, we note that our sample includes the MACS 0416-Y1 source from Laporte et al. (2015) (i.e., id=3107165). This source is extended and has a reported ALMA redshift of $z = 8.3118$ (Tamura et al. 2019). We measure its magnitude in $F444W = 24.74 \pm 0.06$ and its magnification to be $\mu = 1.63 \pm 0.01$, thus meeting the selection criteria even accounting for lensing.

3.2 Source fitting

For all sources, we first estimate the redshift either with spectroscopy when available or using a photo- z template-fitting code. Then, the photometry of each source is fit to measure its stellar mass, accounting for the magnification of the nearby cluster, as described in detail below.

3.2.1 Spectroscopy fitting

The sources selected in the cluster fields have been observed with NIRISS. However, inspection of the NIRISS data shows that none of the double-break sources have a strong enough detected signal to measure a redshift. Therefore only NIRSpec spectroscopy is considered in the rest of this work.

Among our sample of 19 double-break galaxies, five galaxies were observed with NIRSpec. Their 1D and 2D spectra are shown in Fig. 3. Our goals with spectroscopic observations in this paper are to obtain the spectroscopic redshifts (spec- z) and to estimate the effect of emission lines on photometry in filters where the Balmer breaks are possibly captured (i.e., F410M and F444W; their transmission curves are also shown in Fig. 3 with blue and red solid lines, respectively). Thus, we focused particularly on emission lines observed at $3.8 \mu\text{m}$ to $5.0 \mu\text{m}$, wavelengths that these two filters cover.

Four of the five galaxies have obvious detections of

² The photometry and fit properties of the candidate sources can be found on <https://niriss.github.io/doublebreak.html>

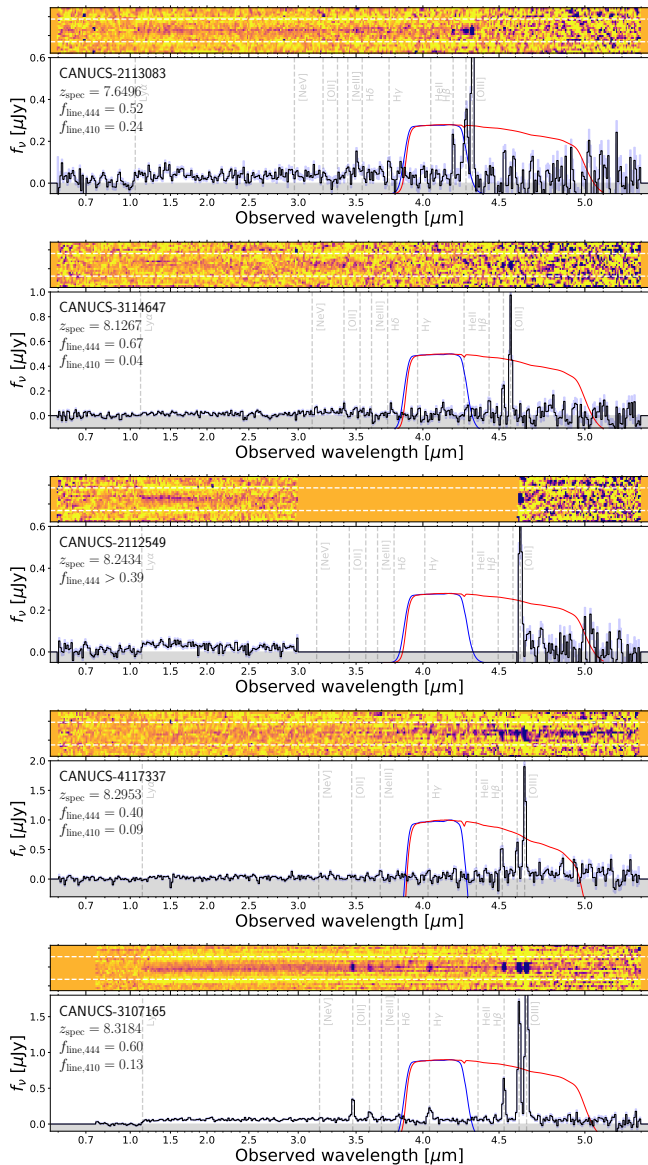


Figure 3. NIRSpec observations of the five targeted double-break sources. The spectra show the fractional contributions to the F410M (blue) and F444W (red) NIRCam filter photometry from strong emission lines. All five galaxies have strong emission lines, especially [OIII], making up $\sim 50\%$ of the F444W filter flux.

[OIII] $_{\lambda 4959, \lambda 5007} + H_{\beta}$ emission lines in this wavelength range, so we first measured the spectroscopic redshifts and the emission line fluxes by performing Gaussian profile fitting on the 1D spectra. Errors are estimated by perturbing the observed 1D spectra within associated errors and repeating the Gaussian fit a 1000 times, and measuring the 16th and 84th percentiles. We do not include any potential systematic errors here – these are difficult to estimate but are likely present given the reported offsets of $\delta z = 0.004$ between NIRSpec prism and grating spectra (Bunker et al. 2023a). In cases where other, fainter emission lines can be seen in the 2D spectra in the target wavelength range (e.g., H_{γ}), we also fit Gaussian profiles to these lines while fixing the redshift to obtain their line fluxes. We then derived the total fluxes in each of the F410M and F444W filters by integrating the observed spectrum through the filter transmission curves, and calculated ratios of emission-line fluxes to the total broadband fluxes

to derive the flux fractions contributed by the emission lines in the F410M and F444W filters. It is worth noting that we did not make slit-loss corrections in this analysis, but slit-loss corrections are not expected to significantly affect the spectroscopic redshifts or emission line flux fractions. The resulting spectroscopic redshifts and emission line flux fractions in the F444W filter ($f_{\text{line},444}$) and in the F410M filter ($f_{\text{line},410}$) are shown in Fig. 3 and Tab. A1. One of the five galaxies (id=3107165) and the ALMA spectroscopic redshift was reported to be $z_{\text{spec}} = 8.3118$ (Tamura et al. 2019, source MACS 0416-Y1), although with some variation over $z = 8.3113$ – 8.3125 (Bakx et al. 2020; Tamura et al. 2023). Our NIRSpec redshift of this galaxy is $z_{\text{spec}} = 8.3184 \pm 0.0001$ which is close to but formally discrepant with the ALMA redshift due to our small fit error. Accounting for a possible systematic error in the NIRSpec measurement (Bunker et al. 2023a) results suggest this may be $\delta z \sim 0.004$ would give ALMA-JWST redshift agreement at the $\sim 2\sigma$ level.

We have one source (id=2112549) whose emission lines mostly fall inside the NIRSpec detector gap. Only one strong emission line at $\lambda_{\text{obs}} \sim 4.6 \mu\text{m}$ is found – at the edge of the detector but detected at high significance in spite of the proximity to the detector edge. In addition to this line, the spectrum of this source also shows a clear break at $\lambda_{\text{obs}} \sim 1.1 \mu\text{m}$. This Lyman break would exactly match up with the strong emission line being [OIII] $_{\lambda 5007}$ at $z = 8.2434 \pm 0.0011$. We thus fit a single Gaussian profile to the emission line, whose peak and part of blue wing lie on the detector. Since other strong emission lines that fall into the detector gap, such as H_{β} , are expected to be covered with the F410M/F444W filters, it is impossible to estimate the contributions of all emission lines to the total fluxes in these filters. For this galaxy, we therefore used the measured [OIII] $_{\lambda 5007}$ line flux and estimated its [OIII] $_{\lambda 4959}$ flux by assuming [OIII] $_{\lambda 5007}$ /[OIII] $_{\lambda 4959} = 3.0$, and took the ratio to the $0''.3$ -diameter aperture flux in F444W from photometry to obtain the lower limit of $f_{\text{line},444}$.

3.2.2 Photometry fitting

First, we fit the source SEDs to derive their photometric redshifts. For that task, we use the Phosphoros template-fitting code (Euclid Collaboration: Desprez et al. 2020; Paltani et al., in prep.). As we are dealing with high- z candidates, we modify the Phosphoros configuration defined in Desprez et al. (2023) to better account for such type of objects. Thus, in addition to the 33 COSMOS templates (Ilbert et al. 2013), we fit the Larson et al. (2023) SED templates (sets 1 and 4). For these templates, intrinsic extinction is allowed to vary in a similar way as for the COSMOS starburst templates, with a reddening excess E(B-V) ranging from 0–0.5 and with two versions of the Calzetti et al. (2000) law with both with the 2175Å bump, using two different bump intensities. A prior on all the SEDs is set, weighting their fit results according to their colour-space coverage, thus avoiding over-weighting some solutions due to SEDs that are too similar to each other. No prior is set on source magnitudes to avoid forcing low redshift solutions on what could be highly unusual high- z sources. Redshift probability distribution functions, $P(z)$, are then estimated over $z = 0$ – 15 with $\delta z = 0.01$ steps. The resulting $P(z)$ are shown in Fig. 4, A2, A3, and A4.

To ensure the quality of the fit photo- z , we compare Phosphoros results to those of EAZY (Brammer et al. 2008). Here, the CANUCS photometry is fit by the standard EAZY templates (tweak_fsps_QSF_12_v3) augmented with the Larson et al. (2023) templates. The results of the best fit EAZY redshifts are shown in Fig. 4 (and in all figures in Appendix A) along with the Phosphoros results, and show good agreement between the two codes. We also use EAZY to test the brown dwarf hypothesis for source id=4115596.

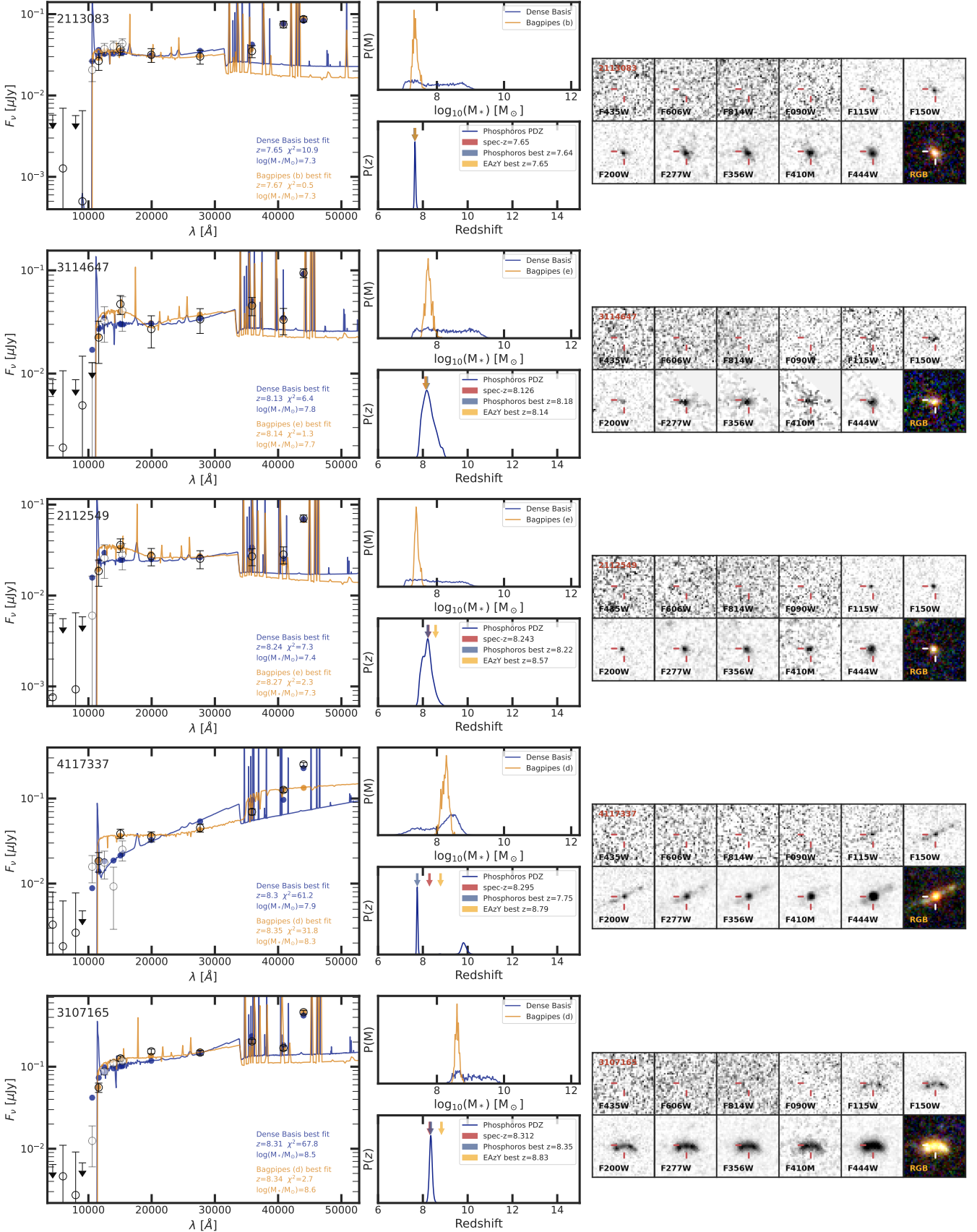


Figure 4. Observed SEDs, fits, and image stamps for the five CANUCS double-break sources observed with NIRSpect. The best model fits of both Dense Basis (blue) and Bagpipes (orange) are displayed, with the SED-fitting redshift and stellar mass posteriors. In the case of Bagpipes, only the best fit configuration (noted a, b, c, d, or e) is shown. The redshift sub-panels show the Phosphoros $P(z)$ (blue curve), and the arrows indicate the Phosphoros (blue) and EAzy (orange) best fit redshifts and the spec- z (red). The stamps show the sources in the *HST* optical bands and *JWST* bands.

For this, we fit the Sonora [Marley et al. \(2021\)](#) cool brown dwarf templates to the photometry. The comparison of the best fit χ^2 of these brown dwarf templates ($\chi_{\text{BD}}^2 = 10$) to that for the EAZY galaxy templates ($\chi_{\text{gal}}^2 = 62$), along with those of Dense Basis and Bagpipes (see Fig A1) confirms our decision to discarding this source from our sample. All other sources in our sample were also fit with these brown dwarfs models as a test, but they all have $\chi_{\text{BD}}^2 > 60$) and all are much better fit by high-redshift galaxy templates.

Next, all sources are fit using Dense Basis (hereafter DB, [Iyer & Gawiser 2017](#); [Iyer et al. 2019](#)) to determine their stellar masses. A collection of DB atlases is created for all redshifts on the same grid as for the Phosphoros $P(z)$. These atlases are designed to contain 10 000 template SEDs, running mostly with the default DB configuration, except for two priors: that of the star formation rate prior, which is set to be flat between 10^{-1} – $10^3 \text{ M}_{\odot} \text{ yr}^{-1}$, and that of the mass prior, whose lower limit is set to $M_{*,\text{min}} = 10^7 \text{ M}_{\odot}$. For each source, a sample of 100 redshifts is randomly drawn using the Phosphoros $P(z)$ as a prior, or the spec- z when available and its photometry is fit to the DB atlases. The cluster magnification is corrected for in each fit result by randomly selecting one instance of the lensing model and measuring the expected magnification for the fit redshift. Combining all the fit results allows us to build a probability distribution function for the mass, $P(M)$, that accounts for both redshift and magnification uncertainties. The mass $P(M)$ are shown in Fig. 4, A2, A3, and A4.

To ensure that our DB results can be compared properly to the masses in L23, we also fit the photometry of the L23 sources following the same steps as described before. We use Phosphoros to derive their photo- z and $P(z)$, and we fit their photometry with DB to obtain their stellar masses. Two of the L23 sources have spectroscopic redshifts: source id=39575 has $z = 7.9932$ ([Fujimoto et al. 2023](#)) and source id=13050 has $z = 5.624$ ([Kocevski et al. 2023](#)). Due to its lower spec- z and broad line AGN component, source id=13050 has been discarded from the comparisons. For source id=39575, the stellar mass has been measured with DB at its spec- z . The results of the fits are presented in Table A1.

Another set of fits for our sample objects is done using the Bayesian analysis of galaxies for physical inference and parameter estimation software (Bagpipes, [Carnall et al. 2018](#)) following a similar procedure as that outlined in L23. The sources are fit using five different configurations used by L23, but their redshifts are fixed to their spec- z , when available, or at the best-fit redshifts (lowest χ^2) from Phosphoros, only allowed to vary according to a Gaussian prior with $\sigma_z = 0.05$. The configurations are: Bagpipes_csf_salim (noted *a*), Bagpipes_rising_salim (*b*), Bagpipes_csf_salim_logage (*c*), Bagpipes_csf_salim_logage_snr10 (*d*), and Bagpipes_csf_smc_logage (*e*), and we refer to L23 for the configuration details. The fit results from the five Bagpipes configurations are combined as follows: the stellar mass reported is the median of all results, and the error limits are given by the lowest and highest results.

3.3 Results

The resulting stellar masses and redshifts for the CANUCS double-break sample are presented in Fig. 5 and Table A1. Figure 5 also shows the results from L23, corrected for the difference in IMF. We note that the CANUCS double-break population remains under the mass threshold of $10^{10} \text{ M}_{\odot}$, regardless of the code used for the fit. We find that the majority of our sources have a photometric redshift $z < 9$, with the exception of one source (id=3102668) which has a broad Phosphoros $P(z)$ leading to a large discrepancy between the

best-fit redshift and the $P(z)$ median. This outlier also presents the highest computed mass with DB, with $M_* = 7.9_{-4.0}^{+4.6} \times 10^9 \text{ M}_{\odot}$. The median stellar mass of the CANUCS sample is $M_* = 2.0 \times 10^8 \text{ M}_{\odot}$ with DB and $M_* = 7.6 \times 10^7 \text{ M}_{\odot}$ with Bagpipes. We note that despite having samples of sources with similar luminosities and colors (see Fig. 2), CANUCS galaxies seems to be generally less massive than the CEERS ones.

The solid curves in the right panel of Fig. 5 show the cumulative source density vs. stellar mass for the different samples and mass fitting procedures. We note a discrepancy between the densities of the L23 (blue line) and CANUCS Phosphoros+DB (red line) samples of roughly ~ 0.8 dex in stellar mass. We also see that the CANUCS Bagpipes fits (orange line) provide a lower source density for a given stellar mass than the Phosphoros+DB fits, but the difference is mainly due to the most massive source with the uncertain redshift. Figure 5 right panel also shows the individual cumulative mass densities for the different CANUCS line-of-sights from the Phosphoros+DB results. The different field densities exhibit a large scatter, with differences up to ~ 1.5 dex at fixed density. We note that the density of the L23 sample is reached by the densest CANUCS fields, but this is mainly due to sources with high photo- z ($z_{\text{phot}} > 8.5$ values whose redshift and masses are uncertain (see Sect. 4.2).

From the DB and Bagpipes fit results, we build the cumulative stellar mass density function of our double-break sample. We focus only on redshifts $z \sim 8$, comparable to L23's $z = 7.0$ – 8.5 range, as this is where the majority of our sample is. For higher redshifts the limited size of our (and L23's) sample would not allow a meaningful comparison. Following L23, in Figure 6 we show the L23 cumulative stellar mass density along with CANUCS cumulative stellar mass densities computed with both our template fitting codes, and the results of our Phosphoros+DB fitting of the L23 sample photometry. The Figure also displays the [Stefanon et al. \(2021\)](#) estimation of the $z \sim 8$ cumulative mass density function derived with *HST* and *Spitzer*/IRAC.

The contours presented in Fig. 6 represent the 1- and 2- σ errors on the position of the cumulative stellar mass density functions. For the CANUCS samples, they are computed from randomly sampling the joint mass, redshift and magnification posteriors with 10 000 draws, and building as many cumulative functions considering random sub-samples of the full dataset while accounting for fitting errors and for field-to-field variance in the survey. For the CEERS sample fit with Phosphoros+DB, we also draw 10 000 samples from the joint mass and redshift posteriors, although we cannot include field-to-field variance in the same way as we do for CANUCS since the CEERS data cover only one field. Instead, we use bootstrap resampling to account for sample variance. The contours are then built using kernel density estimate with Scott's rule ([Scott 1992](#)), encompassing 68 and 90 per cent of the random cumulative mass density point positions.

Figure 6 shows that our Phosphoros+DB fit results for the CEERS sample are consistent with those in L23. We also note that there is good agreement between our two fitting procedures for the CANUCS sample. However, the CEERS and the CANUCS samples provide density distributions that are quite different, the CEERS one lying above the [Stefanon et al. \(2021\)](#) distribution, and the CANUCS one below it. We note that the cumulative distributions are mainly driven by their respective most massive points, which is reflected in the bimodality in mass density error contours for the lower-mass population of the samples. Both the CEERS sample and the CANUCS Bagpipes sample display this multi-modal error distribution due to the presence of one massive outlier in each sample. In the case of the CEERS sample, the mode corresponding to the situation where the

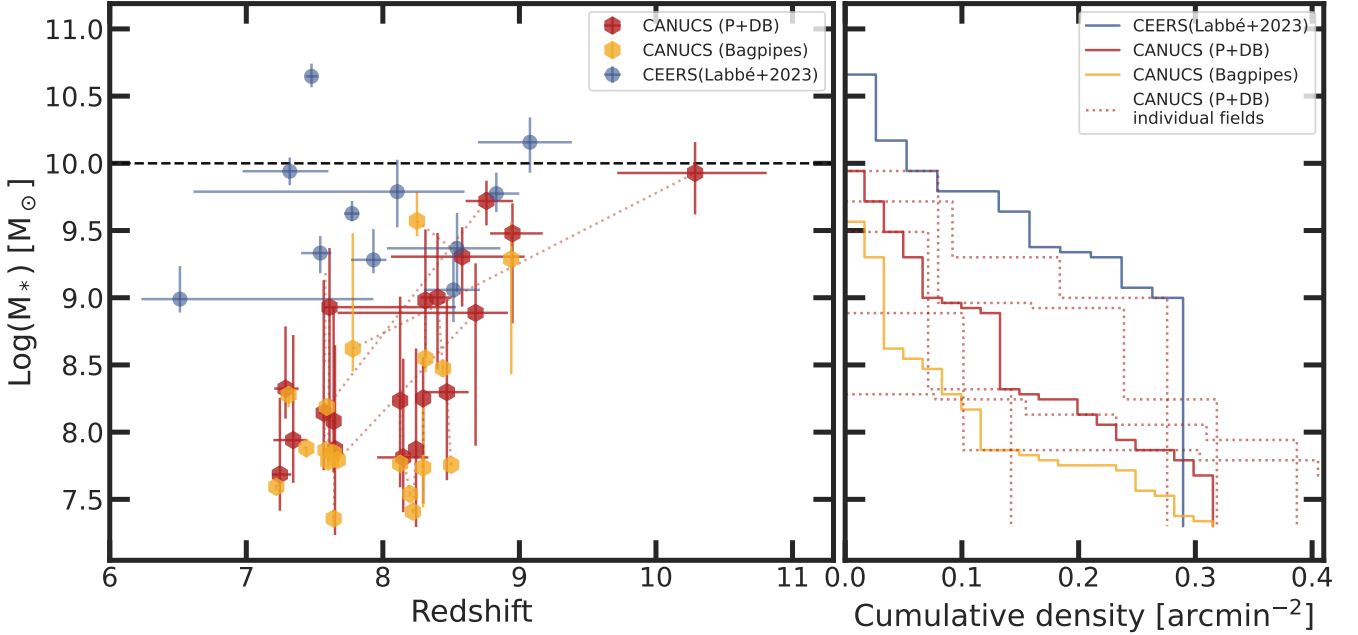


Figure 5. Stellar masses versus redshift (left) and cumulative mass density by decreasing stellar mass (right). In the left panel, the CANUCS sample Phosphoros+DB redshifts and mass (red hexagons) and the *Bagpipes* ones (orange hexagon) are compared to the CEERS L23 sample with masses scaled from [Salpeter \(1955\)](#) to [Chabrier \(2003\)](#) IMF (blue circles). As *Bagpipes* and DB do not use the same redshift in the fits, the former using only the Phosphoros best fit redshift, where the latter uses the full $P(z)$ (represented in this panel by the median point estimate), their redshift value differs. Thus the dotted lines link the two code results for the same sources. In the right panel, the distribution of cumulative density of sources ranked by stellar masses are shown for both samples and both mass estimates in the CANUCS case. The red dotted lines in the right panel show the cumulative densities for each of our five clusters (*CLU+NCF* fields) separately using the DB results, illustrating the large field-to-field variance in the number densities.

massive source is absent from the resampling (shown with lighter-coloured blue crosses) lies close to the *HST*+*IRAC* cumulative distribution.

In contrast to the CEERS sample, the CANUCS sample lies below the [Stefanon et al. \(2021\)](#) *HST*+*IRAC* curve in all cases. This is not unexpected: Since there is no reason to think that our sample is complete (it is designed to selected double-break sources only, whilst the [Stefanon et al. \(2021\)](#) curve has no such restriction), it is expected that the CANUCS cumulative double-break source mass distributions are lower limits on the total population. They are expected to fall below those for the more complete sample from *HST*+*IRAC*. It is the fact that the CEERS double-break sample lies above the *HST*+*IRAC* curve that has been regarded as at odds with previous observations, although – as we have argued above – removing the most massive, extreme outlier from that sample goes a long way towards reconciliation with previous, pre-*JWST* observations.

4 DISCUSSION

The physical properties of the high- z double-break source population has been claimed to be in tension with the Λ CDM cosmology. This is mainly due to the assumption that this population represents the most massive end of the high redshift population due to their brightness and the putative presence of the Balmer break that indicates an evolved and massive stellar population. Despite finding in CANUCS sources with similar SED properties in terms of brightness and colours, we do not find stellar masses that appear to be in tension with pre-*JWST* literature and cosmology predictions. We discuss here the different

reasons that explain why the double-break galaxy population seems not to be problematic from the analysis carried out in this work.

4.1 Emission lines rather than Balmer Breaks

Double-break photometric selection criteria can select several types of sources ([Barro et al. 2024](#); [Trussler et al. 2023](#)): for some the red break can be the Balmer break due to evolved stellar populations; for some, strong optical emission lines can masquerade as a break in the photometry ([Schaerer & de Barros 2009](#)); and some can be red AGN at high- z ([Matthee et al. 2023](#); [Labbe et al. 2023a](#)). The Balmer break galaxies will have greater stellar masses than those dominated by emission lines or an AGN component, so knowing the nature of the photometric break is a strong requirement to ensure the validity of the mass measurements. However, at most redshifts, broad band photometry alone is insufficient to break these degeneracies. To break the degeneracies either spectroscopy or medium band photometry is needed.

Our sample of double-break sources has been selected through the same photometric criteria prescribed by L23 (Section 3.1). All double-break sources present in the *CLU* fields were identified as high priority candidates for spectroscopic follow-up, but due to limitations on slit positions imposed by the three MSA configurations per *CLU* field centred on the cluster, only five of these were observed. Given the MSA assignment procedure, there is no reason to think that these five are in any way systematically different than the full sample. The spectra of all five (Fig 3) show strong [OIII] and $H\beta$ emission lines that fall in the F444W band. Moreover, no Balmer breaks are visible in the continua, although in some cases the continuum S/N

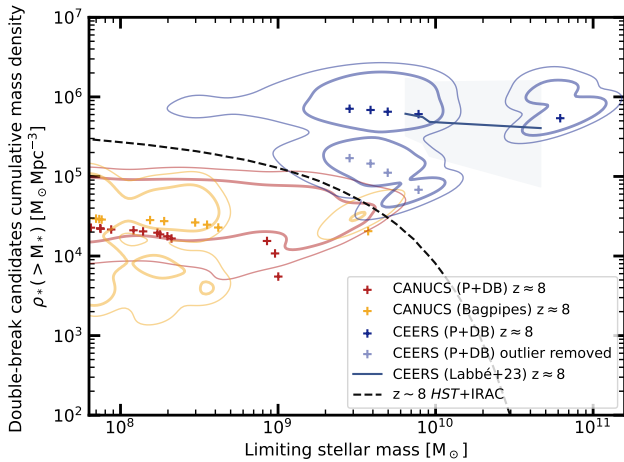


Figure 6. Cumulative stellar mass densities of the double-break source samples in the redshift range $z = 7\text{--}8.5$. The CANUCS sample results are shown by the red crosses for the cumulative mass densities obtained with DB and the orange crosses for *Bagpipes*. The CEERS sample **L23** results are displayed as the blue line and the blue crosses show the results obtained with DB on that sample. The light shade blue crosses show the CEERS sample Phosphoros+DB results while removing the contribution of the most massive source. The coloured contours represent the one (thick contours) and two σ (thin contours) errors on the positions of the different cumulative distribution points computed from resampling. The visible offset of the contours from the points is expected and is due to the population of higher redshift and more massive sources that can fall in the $z \sim 8$ range during the random resampling. Inversely, the different modes in the contours are due to the most massive, outlier object in the $z \sim 8$ sample leaving during the resampling, thereby leaving only the less massive population. The dashed black line show the expected stellar mass density at $z \sim 8$ from *HST* and *IRAC* observations (Stefanon et al. 2021). The masses are all scaled to the Chabrier (2003) IMF.

is low. The estimated contributions of the emission lines to the observed broadband F444W fluxes range from ~ 40 to 70 percent, thus explaining the apparent break observed in the photometry.

In the CEERS double-break sample, one source has been observed with NIRSpec and has been confirmed to be at redshift $z = 7.9932$ (Fujimoto et al. 2023). Similarly to our objects, the reported spectrum also shows strong [OIII] and $H\beta$ lines in the F444W wavelength range.

While we cannot rule out that other galaxies in the double-break sample do not have Balmer breaks, the fact that for all our observed sources spectra are from break-less line emitters seems to indicate that emission lines, rather than Balmer breaks, are a more plausible cause of the observed photometric breaks. The SED fits of some CANUCS galaxies show that both solutions are plausible with DB and *Bagpipes* proposing both solutions as best fits (e.g., id=1111752, id=1211968 or id=4117337). In the absence of spectroscopy the emission line/Balmer break degeneracies in these objects cannot be resolved. Consequently, spectroscopy is required to confirm the nature of all double-break sources (Roberts-Borsani et al. 2020); alternatively, medium band photometry could be used to properly sample the red parts of the SEDs (Trussler et al. 2023). Our results are in line with other *JWST* photometric and spectroscopic studies that suggest strong rest-optical emission lines are more common than strong Balmer breaks (Endsley et al. 2023a; Vikaeus et al. 2024) at the relevant redshifts.

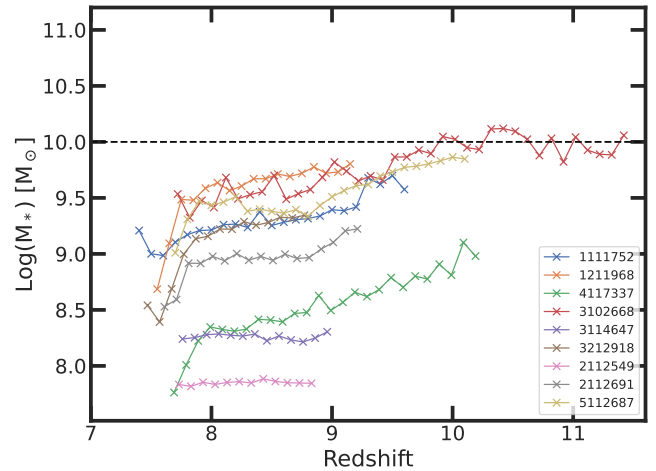


Figure 7. Covariance between stellar mass and redshift in Dense Basis fits for sources with a broad $P(z)$. In most cases, a higher mass is obtained at a higher redshift. Some sources show a steepening at $z > 9$ where the strong [OIII] lines move out of the F444W filter.

4.2 Getting the right redshift

To properly assess the stellar masses of galaxies, a reasonable knowledge of the redshift is required, as the mass fits depend on the proper identification of SED features (i.e., Balmer break position and strength) as well as intrinsic brightness of the sources. For instance, Fig. 7 shows how the stellar masses vary with the redshift for the CANUCS double-break objects within the broad range of redshift allowed by their Phosphoros+DB $P(z)$'s. The Figure illustrates that changing the redshifts moves the positions and strengths of the emission lines and Balmer breaks as the SEDs move through the filters, resulting in higher inferred masses for higher redshifts. In particular, some sources show a steepening at $z > 9$ where the strong [OIII] lines move out of the F444W filter. For example, source id=4117337 has a spectroscopic redshift at $z = 8.295$, and a stellar mass fit of $\log(M_*/M_\odot) \sim 8.3$ with DB at this redshift. Nevertheless, Fig. 4 shows that Phosphoros $P(z)$ allows for a solution around $z \sim 9.7\text{--}10$, matching a fit of the SED red break with a Balmer break. For these redshift, Fig. 7 shows that the stellar mass fit becomes $\log(M_*/M_\odot) \sim 8.8$, thus a 0.5 dex increase. However, this value is source dependant as it depends on the strength of the emission lines and thus cannot be generalised to the whole sample, but it gives an insight of the correction that can be expected for such effect. This can also explain some differences between the DB and *Bagpipes* results, as they do not use the same redshifts (*Bagpipes* uses the best-fit redshift, which is generally lower than the median redshift, thus leading to lower stellar masses).

Selection from broadband photometry can lead to the inclusion of outliers in the sample – outliers for which the photo- z is strongly discrepant with the true redshifts. This is the case for the CEERS source id=13050 in **L23**, with a photo- z estimated at $z_{\text{phot}} = 8.14^{+0.45}_{-1.71}$ and a stellar mass of $\log(M_*/M_\odot) = 9.9^{+0.29}_{-0.3}$ but for which spectroscopic observations showed it to be an AGN at $z_{\text{spec}} = 5.624$ (Kocevski et al. 2023). This underlines the importance of obtaining spectroscopy for individual high- z candidates in order to properly characterise the masses (and other properties) of the population. To emphasise: even though the photometric redshifts may be approximately correct, exact, spectroscopic redshifts are needed for unbiased mass determinations.

4.3 Field-to-field variance

With five widely separated sight-lines, the CANUCS data in Fig. 5 and Table 1 show different numbers of objects and stellar mass densities in each field. Figure 5 (right panel) shows that there is a difference up to ~ 1.5 dex in stellar mass between the most massive double-break sources found in the five different fields. The CEERS field presents a higher mass density than any of the CANUCS fields, and has a mass difference of ~ 0.5 to 1.0 dex with the whole CANUCS sample at fixed source density and considering only the most massive estimates for our sample. Although there may be minor systematic differences between the CANUCS and CEERS samples due to data quality (CANUCS is deeper and has more *JWST* filters) and SED fitting procedures (Sections 3.3, 4.1, 4.2), it does indeed appear that the four CEERS NIRC*am* pointings analysed by L23 are more over-dense in massive galaxies at this redshift than the typical random sight-lines probed by CANUCS.

The variance in mass density observed in these fields is a combination of sample variance and cosmic variance. For the five CANUCS sight-lines, the number of sources observed ranges between 2 and 5. This level of variation could be completely explained by Poisson variance. The higher mass density from CEERS is likely at least partially a consequence of cosmic variance. L23 estimate the effect of cosmic variance in their sample to be 30%, but along a single sight-line there will always be an element of uncertainty in such a calculation. For example, the GLASS NIRC*am* parallel field shows a $3\times$ to $10\times$ overdensity in galaxies at redshift $z \sim 10$ (Castellano et al. 2023). High-redshift overdensities have also been observed in *JWST* spectroscopic samples (Kashino et al. 2023; Morishita et al. 2023; Helton et al. 2024), as expected based on the growth of large-scale structure. The CANUCS results presented here show that typical sight-lines do not show a high mass density at these redshifts and serve as a caution that multiple fields should be considered before drawing strong conclusions about what is typical.

4.4 Effect of outlier(s)

The cumulative stellar mass density distributions presented in Fig. 6 depend strongly on the most massive object in the sample. This is especially the case when a single source is an outlier. This is illustrated by the error contours in the figure showing that in the presence of such massive outliers, a multi-modal distributions results, as is the case for the CEERS sample DB results and for the CANUCS *Bagpipes* ones. This is due to the potential absence of outlier sources in the resampling used to create the contours, thus leading to cumulative distributions only considering the lower mass sample. This is further illustrated for the CEERS sample with lighter shade crosses in the Fig 6, showing what the cumulative mass density would be without the most massive source in the sample. Disregarding the most massive source, the results of the CEERS sample are consistent with the Stefanon et al. (2021) stellar mass density distribution, as suggested by Akins et al. (2023) or Wang et al. (2023b). We note that we can see a similar effect for the *Bagpipes* results on the CANUCS sample that is due to source id=1111752, which is more massive than the rest of the $z \sim 8$ sample by 0.7 dex. Disregarding this outlier would draw the density distribution down, but it would still remain consistent with the results of *Phosphoros*+DB. This is not a problem, as we expect that the CANUCS sample of double-break galaxies is only a subset of all $z \approx 8$ objects.

The effect of these outliers is problematic in small samples and small probed volumes regardless of their true nature. It could be that these massive sources are indeed truly massive Balmer break galax-

ies, but the size of the samples and the volume which is probed are too limited to allow generalising the results obtained with proper statistical significance. As discussed in the previous section (Sect. 4.3), cosmic variance is an explanation of the potential presence of such outliers in the sample. Larger areas in different, widely-separated sight-lines need to be probed to determine whether the high stellar mass densities they result in are real or just an artefact of the small samples used to measure the average mass density.

Outliers can also be due to a miss-classification of sources (AGN, brown dwarf, etc.), or even improper fits of their SEDs, as discussed in the previous sections (see Sect. 4.1 and 4.2). One example of this is CANUCS source id=4115596, whose colours match the double-break criteria but which seems to be a brown dwarf. Including it in the analysis would have added a source with $M_* = 0.3^{+3.7}_{-0.2} \times 10^9 M_\odot$ according to DB and $M_* = 2.5^{+3.8}_{-2.2} \times 10^9 M_\odot$ from *Bagpipes* (see Fig A1), which would have resulted in a massive outlier in the sample. Another example in the literature, the Endsley et al. (2023b) fit of the most massive galaxy of L23 suggests that after accounting for emission lines and/or AGN emission, the stellar mass of the source drops by one dex and the source ceases to be an extreme massive galaxy. Sources where the double-break signature has been revealed to be AGN or brown dwarfs (Greene et al. 2023; Kokorev et al. 2023; Labbe et al. 2023a; Langeroodi & Hjorth 2023; Burgasser et al. 2024) should be considered to be such miss-classified outliers.

5 CONCLUSIONS

This work presents an analysis of double-break sources in the CANUCS survey. Over the effective area ~ 60 arcmin² for $z \sim 8$ covering five cluster and parallel fields, we detect 20 sources that correspond to the double-break criteria as defined by L23. Removing one brown dwarf from this sample, we are left with 19 double-break galaxies. The redshifts and stellar masses of these 19 galaxies are derived with a combination of *Phosphoros* and either *Dense Basis* or *Bagpipes*. The stellar masses obtained are compared to the ones of the CEERS sample and are found to be lower, and not in contradiction with the stellar mass densities derived with *HST* (Stefanon et al. 2021) or with galaxy formation models in standard Λ CDM (Menci et al. 2022; Lovell et al. 2023). In other words, CANUCS does not find a large population of massive Balmer-break sources at high z .

The difference between the conclusion from the CANUCS sample and that of CEERS can be explained by a combination of four different effects. The first one is the confusion between the contribution of optical emission lines and the Balmer break produced by an evolved galaxy population in the source SEDs. Out of the 19 candidates in our sample, five are observed with NIRS*pec* and all five of these spectra present strong emission lines that contribute strongly to the red band fluxes. Whilst this does not discard the possibility that other sources in our sample may have pronounced Balmer breaks, emission lines seem more likely to explain the photometry break than an old and massive stellar population at high- z .

Secondly, a precise knowledge on the source redshift is necessary, as the mass can strongly vary with the redshift assumed, especially when strong emission lines (or a pronounced Balmer break) are moving in and out of photometric bands. Thus, unconstrained $P(z)$ can lead to poorly constrained stellar mass estimates.

Thirdly, field-to-field variance plays a role as we observe significant variation in the properties of the double-break population from one CANUCS field to another, and see an even higher mass density in the CEERS field used by L23. A single narrow sight-line is not

enough to generalise the properties of the population found in it to the entire universe.

Finally, when handling small samples, the cumulative stellar mass density distribution is highly dependent on the most massive object used to build it, and thus is extremely sensitive to outliers. Whether those outliers are truly rare massive sources, misclassified lower z interlopers, unaccounted-for AGN, brown dwarfs, or even bad fit results, the cumulative mass distribution is driven by their upward reported masses.

In order to claim that the observed population of high- z galaxies is in tension with our expectations from Λ CDM, all these points must be addressed. Deep spectroscopy over large areas and different sight-lines in addition to deep broad and medium band photometry are needed to ensure the robustness of the conclusion drawn about the high-end of stellar mass density at $z > 7$.

ACKNOWLEDGEMENTS

The authors thank the referee for their helpful comments. This research was enabled by grant 18JWST-GTO1 from the Canadian Space Agency, and Discovery Grants to MS, AM, and RA from the Natural Sciences and Engineering Research Council (NSERC) of Canada. YA is supported by a Research Fellowship for Young Scientists from the Japan Society of the Promotion of Science (JSPS). MB and GR acknowledge support from the ERC Grant FIRSTLIGHT and from the Slovenian national research agency ARRS through grants N1-0238 and P1-0188. MB acknowledges support from the program HST-GO-16667, provided through a grant from the STScI under NASA contract NAS5-26555. This research used the Canadian Advanced Network For Astronomy Research (CANFAR) operated in partnership by the Canadian Astronomy Data Centre and The Digital Research Alliance of Canada with support from the National Research Council of Canada the Canadian Space Agency, CANARIE and the Canadian Foundation for Innovation.

DATA AVAILABILITY

The CANUCS data is available at DOI: 10.17909/ph4n-6n76. The data presented in this work will be provided on request.

REFERENCES

- Akins H. B., et al., 2023, *ApJ*, 956, 61
 Arrabal Haro P., et al., 2023, *Nature*, 622, 707
 Asada Y., et al., 2023, *MNRAS*, 523, L40
 Asada Y., et al., 2024, *MNRAS*, 527, 11372
 Atek H., et al., 2023, *arXiv e-prints*, p. arXiv:2308.08540
 Bagley M. B., et al., 2023, *ApJ*, 946, L12
 Bakx T. J. L. C., et al., 2020, *MNRAS*, 493, 4294
 Barro G., et al., 2024, *ApJ*, 963, 128
 Bergamini P., et al., 2023, *A&A*, 674, A79
 Biagetti M., Franciolini G., Riotto A., 2023, *ApJ*, 944, 113
 Boylan-Kolchin M., 2023, *Nature Astronomy*, 7, 731
 Bradley L., et al., 2023, *astropy/photutils*: 1.7.0, doi:10.5281/zenodo.7804137, <https://doi.org/10.5281/zenodo.7804137>
 Brammer G., 2022, gbrammer/msaexp: Full working version with 2d drizzling and extraction, doi:10.5281/zenodo.7299501, <https://doi.org/10.5281/zenodo.7299501>
 Brammer G., 2023, grizli, Zenodo, doi:10.5281/zenodo.8210732, <https://doi.org/10.5281/zenodo.8210732>
 Brammer G. B., van Dokkum P. G., Coppi P., 2008, *ApJ*, 686, 1503
 Bunker A. J., et al., 2023a, *arXiv e-prints*, p. arXiv:2306.02467
 Bunker A. J., et al., 2023b, *A&A*, 677, A88
 Burgasser A. J., et al., 2024, *ApJ*, 962, 177
 Calzetti D., Armus L., Bohlin R. C., Kinney A. L., Koornneef J., Storchi-Bergmann T., 2000, *ApJ*, 533, 682
 Carnall A. C., McLure R. J., Dunlop J. S., Davé R., 2018, *MNRAS*, 480, 4379
 Casey C. M., et al., 2023a, *arXiv e-prints*, p. arXiv:2308.10932
 Casey C. M., et al., 2023b, *ApJ*, 954, 31
 Castellano M., et al., 2023, *ApJ*, 948, L14
 Chabrier G., 2003, *PASP*, 115, 763
 Curtis-Lake E., et al., 2023, *Nature Astronomy*, 7, 622
 Dayal P., Giri S. K., 2024, *MNRAS*, 528, 2784
 Desprez G., Richard J., Jauzac M., Martinez J., Siana B., Clément B., 2018, *MNRAS*, 479, 2630
 Desprez G., et al., 2023, *A&A*, 670, A82
 Doyon R., et al., 2023, *PASP*, 135, 098001
 Drlica-Wagner A., et al., 2018, *ApJS*, 235, 33
 Ebeling H., Edge A. C., Henry J. P., 2001, *ApJ*, 553, 668
 Elíasdóttir Á., et al., 2007, *arXiv e-prints*, p. arXiv:0710.5636
 Endsley R., et al., 2023a, *arXiv e-prints*, p. arXiv:2306.05295
 Endsley R., Stark D. P., Whitley L., Topping M. W., Chen Z., Plat A., Chisholm J., Charlot S., 2023b, *MNRAS*, 524, 2312
 Euclid Collaboration: Desprez G., et al., 2020, *A&A*, 644, A31
 Forconi M., Ruchika Melchiorri A., Mena O., Menci N., 2023, *J. Cosmology Astropart. Phys.*, 2023, 012
 Franco M., et al., 2023, *arXiv e-prints*, p. arXiv:2308.00751
 Fujimoto S., et al., 2023, *ApJ*, 949, L25
 Gaia Collaboration et al., 2016, *A&A*, 595, A2
 Gaia Collaboration et al., 2023, *A&A*, 674, A1
 Gardner J. P., et al., 2023, *PASP*, 135, 068001
 Greene J. E., et al., 2023, *arXiv e-prints*, p. arXiv:2309.05714
 Helton J. M., et al., 2024, *ApJ*, 962, 124
 Hoag A., et al., 2017, *Nature Astronomy*, 1, 0091
 Horne K., 1986, *Publications of the Astronomical Society of the Pacific*, 98, 609
 Hütsi G., Raidal M., Urrutia J., Vaskonen V., Veermäe H., 2023, *Phys. Rev. D*, 107, 043502
 Ilbert O., et al., 2013, *A&A*, 556, A55
 Iyer K., Gawiser E., 2017, *ApJ*, 838, 127
 Iyer K. G., Gawiser E., Faber S. M., Ferguson H. C., Kartaltepe J., Koekemoer A. M., Pacifici C., Somerville R. S., 2019, *ApJ*, 879, 116
 Jakobsen P., et al., 2022, *A&A*, 661, A80
 Jauzac M., et al., 2019, *MNRAS*, 483, 3082
 Jullo E., Kneib J.-P., Limousin M., Elíasdóttir Á., Marshall P. J., Verdugo T., 2007, *New Journal of Physics*, 9, 447
 Kashino D., Lilly S. J., Matthee J., Eilers A.-C., Mackenzie R., Bordoloi R., Simcoe R. A., 2023, *ApJ*, 950, 66
 Kneib J. P., 1993, PhD thesis, -
 Kocevski D. D., et al., 2023, *ApJ*, 954, L4
 Kokorev V., et al., 2023, *ApJ*, 957, L7
 Kron R. G., 1980, *ApJS*, 43, 305
 Labbe I., et al., 2023a, *arXiv e-prints*, p. arXiv:2306.07320
 Labbé I., et al., 2023b, *Nature*, 616, 266
 Lagattuta D. J., et al., 2019, *MNRAS*, 485, 3738
 Lagattuta D. J., et al., 2022, *MNRAS*, 514, 497
 Langeroodi D., Hjorth J., 2023, *ApJ*, 957, L27
 Laporte N., et al., 2015, *A&A*, 575, A92
 Laporte N., Ellis R. S., Witten C. E. C., Roberts-Borsani G., 2023, *MNRAS*, 523, 3018
 Larson R. L., et al., 2023, *ApJ*, 958, 141
 Lovell C. C., Harrison I., Harikane Y., Tacchella S., Wilkins S. M., 2023, *MNRAS*, 518, 2511
 Mahler G., et al., 2019, *ApJ*, 873, 96
 Malekjani M., Mc Conville R., Colgáin E. Ó., Pourojaghi S., Sheikh-Jabbari M. M., 2023, *arXiv e-prints*, p. arXiv:2301.12725
 Marley M. S., et al., 2021, *ApJ*, 920, 85

- Martis N. S., et al., 2024, [arXiv e-prints](#), p. [arXiv:2401.01945](#)
- Matharu J., et al., 2023, [ApJ](#), 949, L11
- Matthee J., et al., 2023, [arXiv e-prints](#), p. [arXiv:2306.05448](#)
- Mauerhofer V., Dayal P., 2023, [MNRAS](#), 526, 2196
- Menci N., Castellano M., Santini P., Merlin E., Fontana A., Shankar F., 2022, [ApJ](#), 938, L5
- Morishita T., et al., 2023, [ApJ](#), 947, L24
- Noiro G., et al., 2023, [MNRAS](#), 525, 1867
- Oesch P. A., et al., 2023, [MNRAS](#), 525, 2864
- Oke J. B., Gunn J. E., 1983, [ApJ](#), 266, 713
- Rieke M. J., et al., 2023, [PASP](#), 135, 028001
- Roberts-Borsani G. W., Ellis R. S., Laporte N., 2020, [MNRAS](#), 497, 3440
- Robertson B. E., 2022, [ARA&A](#), 60, 121
- Robertson B. E., et al., 2023, [Nature Astronomy](#), 7, 611
- Salpeter E. E., 1955, [ApJ](#), 121, 161
- Schaerer D., de Barros S., 2009, [A&A](#), 502, 423
- Scott D., 1992, *Multivariate Density Estimation : Theory, Practice and Visualization*. John Wiley and Sons Ltd, [doi:10.1002/9780470316849](#)
- Soucail G., 1987, [The Messenger](#), 48, 43
- Speagle J. S., Steinhardt C. L., Capak P. L., Silverman J. D., 2014, [ApJS](#), 214, 15
- Stefanon M., Bouwens R. J., Labbé I., Illingworth G. D., Gonzalez V., Oesch P. A., 2021, [ApJ](#), 922, 29
- Strait V., et al., 2018, [ApJ](#), 868, 129
- Strait V., et al., 2023, [ApJ](#), 949, L23
- Su B.-Y., Li N., Feng L., 2023, [arXiv e-prints](#), p. [arXiv:2306.05364](#)
- Tamura Y., et al., 2019, [ApJ](#), 874, 27
- Tamura Y., et al., 2023, [ApJ](#), 952, 9
- Trussler J. A. A., et al., 2023, [arXiv e-prints](#), p. [arXiv:2308.09665](#)
- Vikaeus A., et al., 2024, [MNRAS](#),
- Wang D., Liu Y., 2022, [arXiv e-prints](#), p. [arXiv:2301.00347](#)
- Wang P., Su B.-Y., Zu L., Yang Y., Feng L., 2023a, [arXiv e-prints](#), p. [arXiv:2307.11374](#)
- Wang Y.-Y., Lei L., Yuan G.-W., Fan Y.-Z., 2023b, [ApJ](#), 954, L48
- Wang B., et al., 2023c, [ApJ](#), 957, L34
- Wilkins S. M., et al., 2024, [MNRAS](#), 527, 7965
- Willott C. J., et al., 2022, [PASP](#), 134, 025002
- Windhorst R. A., et al., 2023, [AJ](#), 165, 13
- Withers S., et al., 2023, [ApJ](#), 958, L14
- Xiao M., et al., 2023, [arXiv e-prints](#), p. [arXiv:2309.02492](#)

APPENDIX A: FULL SAMPLE PROPERTIES

In this appendix, we report the properties of the double-break galaxies obtained through fitting in Table A1. We also present the photometry, SED fits, stellar mass posteriors $P(M)$ and photo- z $P(z)$ and point estimates for all the source that do not have a spec- z in Fig. A2, A3, and A4. Figure A1 show the fits of the CANUCS source id=4115596 which is suspected to be a cool brown dwarf, and thus display the best model fit of EAzy for brown dwarfs. Finally, Table A2 quotes the measured 3σ depths in $0''.3$ apertures in all bands and fields.

This paper has been typeset from a $\text{\TeX}/\text{\LaTeX}$ file prepared by the author.

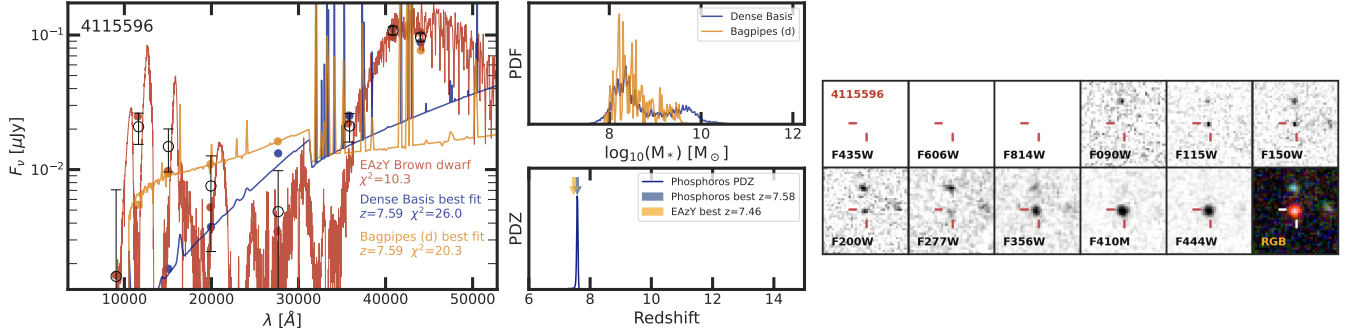


Figure A1. Photometry, SED fit and stamps of the CANUCS source id=4115596 that is much better fit by cool brown dwarf templates than high-redshift galaxy templates.

Table A1. CANUCS and CEERS high- z double-break galaxy fit properties. For CANUCS sources, the first two digits of object ID tag the field+pointing the object belongs to (see Table 1 for field+pointing codes). The reported photo- z results are those of Phosphoros. Bagpipes stellar masses are the median of the 5 configurations, and the given errors are the lowest and highest results of the different configurations.

id	R.A. [deg]	Dec. [deg]	z_{spec}	z_{50}	z_{best}	μ	$\log(M_*/M_\odot)$ DB	$\log(M_*/M_\odot)$ Bagpipes	$f_{\text{line},410}$	$f_{\text{line},444}$
1111752	64.39697	-11.871979	—	$8.58^{+0.46}_{-0.52}$	8.25	$1.559^{+0.056}_{-0.195}$	$9.3^{+0.2}_{-0.4}$	$9.6^{+0.1}_{-0.1}$	—	—
1113392	64.427912	-11.857791	—	$8.4^{+0.1}_{-0.12}$	8.44	$1.118^{+0.011}_{-0.037}$	$9.0^{+0.5}_{-0.5}$	$8.5^{+0.1}_{-0.1}$	—	—
1211968	64.395294	-11.799743	—	$8.76^{+0.2}_{-0.15}$	7.59	$1.046^{+0.004}_{-0.015}$	$9.7^{+0.2}_{-0.2}$	$8.2^{+0.1}_{-0.1}$	—	—
2104427	40.004549	-1.624585	—	$8.15^{+0.18}_{-0.19}$	8.2	$1.517^{+0.031}_{-0.022}$	$7.8^{+0.7}_{-0.4}$	$7.5^{+0.1}_{-0.1}$	—	—
2112549	39.994947	-1.574828	8.2434 ± 0.0011	$8.19^{+0.23}_{-0.23}$	8.22	$2.137^{+0.12}_{-0.053}$	$7.9^{+0.8}_{-0.6}$	$7.4^{+0.1}_{-0.1}$	—	> 0.39
2112691	39.994837	-1.574134	—	$8.68^{+0.24}_{-1.01}$	7.67	$2.133^{+0.111}_{-0.057}$	$8.9^{+0.4}_{-1.0}$	$7.8^{+0.1}_{-0.1}$	—	—
2113083	39.955449	-1.572618	7.6496 ± 0.0005	$7.65^{+0.03}_{-0.03}$	7.64	$2.932^{+0.056}_{-0.053}$	$7.9^{+0.8}_{-0.6}$	$7.4^{+0.1}_{-0.1}$	0.24	0.52
2222435	40.046757	-1.586579	—	$7.25^{+0.08}_{-0.06}$	7.22	$1.196^{+0.008}_{-0.005}$	$7.7^{+0.6}_{-0.3}$	$7.6^{+0.1}_{-0.1}$	—	—
3102668	64.079044	-24.125957	—	$10.29^{+0.52}_{-0.57}$	7.78	$1.099^{+0.002}_{-0.002}$	$9.9^{+0.2}_{-0.3}$	$8.9^{+0.5}_{-0.6}$	—	—
3107165	64.039231	-24.093198	8.3184 ± 0.0001	$8.35^{+0.07}_{-0.06}$	8.35	$1.634^{+0.012}_{-0.009}$	$9.0^{+0.5}_{-0.4}$	$8.5^{+0.1}_{-0.1}$	0.13	0.60
3114647	64.038865	-24.04459	8.1267 ± 0.0006	$8.23^{+0.31}_{-0.24}$	8.18	$1.54^{+0.022}_{-0.009}$	$8.2^{+0.8}_{-0.6}$	$7.8^{+0.1}_{-0.1}$	0.04	0.67
3212918	64.163246	-24.090125	—	$7.61^{+0.92}_{-0.04}$	7.6	$1.049^{+0.001}_{-0.001}$	$8.9^{+0.4}_{-1.1}$	$7.8^{+0.1}_{-0.1}$	—	—
4105584	215.96759	24.071808	—	$7.57^{+0.02}_{-0.03}$	7.58	$1.665^{+0.056}_{-0.118}$	$8.1^{+1.0}_{-0.4}$	$7.9^{+0.1}_{-0.1}$	—	—
4117337	215.944453	24.068738	8.2953 ± 0.0005	$7.78^{+2.09}_{-0.05}$	7.75	$27.808^{+11.826}_{-4.327}$	$8.3^{+0.3}_{-0.8}$	$7.7^{+0.3}_{-0.5}$	0.09	0.40
4201666	215.870262	24.11036	—	$7.34^{+0.1}_{-0.15}$	7.44	$1.023^{+0.002}_{-0.003}$	$7.9^{+0.8}_{-0.3}$	$7.9^{+0.1}_{-0.1}$	—	—
4210883	215.874228	24.162117	—	$7.64^{+0.02}_{-0.02}$	7.64	$1.011^{+0.001}_{-0.002}$	$8.1^{+0.8}_{-0.4}$	$7.8^{+0.1}_{-0.1}$	—	—
4220076	215.860227	24.15628	—	$8.47^{+0.16}_{-0.17}$	8.5	$1.009^{+0.001}_{-0.001}$	$8.3^{+0.7}_{-0.7}$	$7.8^{+0.1}_{-0.1}$	—	—
5112687	177.390929	22.349767	—	$8.95^{+0.22}_{-0.16}$	8.94	$1.057^{+0.001}_{-0.003}$	$9.5^{+0.2}_{-0.7}$	$9.5^{+1.1}_{-0.1}$	—	—
5201389	177.380669	22.268024	—	$7.29^{+0.1}_{-0.08}$	7.31	$1.004^{+0.001}_{-0.001}$	$8.3^{+0.5}_{-0.2}$	$8.3^{+0.1}_{-0.1}$	—	—
2859	214.840534	52.817942	—	$10.21^{+0.69}_{-0.31}$	9.86	—	$10.2^{+0.3}_{-0.3}$	—	—	—
7274	214.806671	52.837802	—	$7.41^{+0.38}_{-0.17}$	7.42	—	$9.7^{+0.1}_{-0.2}$	—	—	—
11184	214.892475	52.856892	—	$7.12^{+0.29}_{-0.14}$	7.11	—	$9.9^{+0.1}_{-0.1}$	—	—	—
14924	214.87615	52.880833	—	$9.36^{+0.73}_{-0.28}$	9.23	—	$10.0^{+0.1}_{-0.2}$	—	—	—
16624	214.844772	52.892108	—	$8.55^{+0.33}_{-0.15}$	8.73	—	$9.4^{+0.3}_{-0.8}$	—	—	—
21834	214.902227	52.93937	—	$10.12^{+0.68}_{-0.32}$	10.12	—	$9.7^{+0.2}_{-0.2}$	—	—	—
25666	214.956837	52.973153	—	$5.59^{+0.02}_{-0.01}$	5.6	—	$8.3^{+0.6}_{-0.2}$	—	—	—
28984	215.002843	53.007594	—	$8.33^{+0.51}_{-0.27}$	8.23	—	$9.6^{+0.1}_{-0.2}$	—	—	—
35300	214.830662	52.887777	—	$9.24^{+0.86}_{-0.39}$	9.16	—	$9.8^{+0.2}_{-0.2}$	—	—	—
37888	214.91251	52.949435	—	$6.57^{+1.76}_{-0.99}$	5.59	—	$9.1^{+0.3}_{-1.1}$	—	—	—
38094	214.983019	52.955999	—	$7.72^{+0.3}_{-0.14}$	7.67	—	$10.8^{+0.1}_{-0.1}$	—	—	—
39575	215.0054	52.996706	7.993	$10.26^{+1.77}_{-1.25}$	8.97	—	$9.5^{+0.2}_{-0.6}$	—	—	—

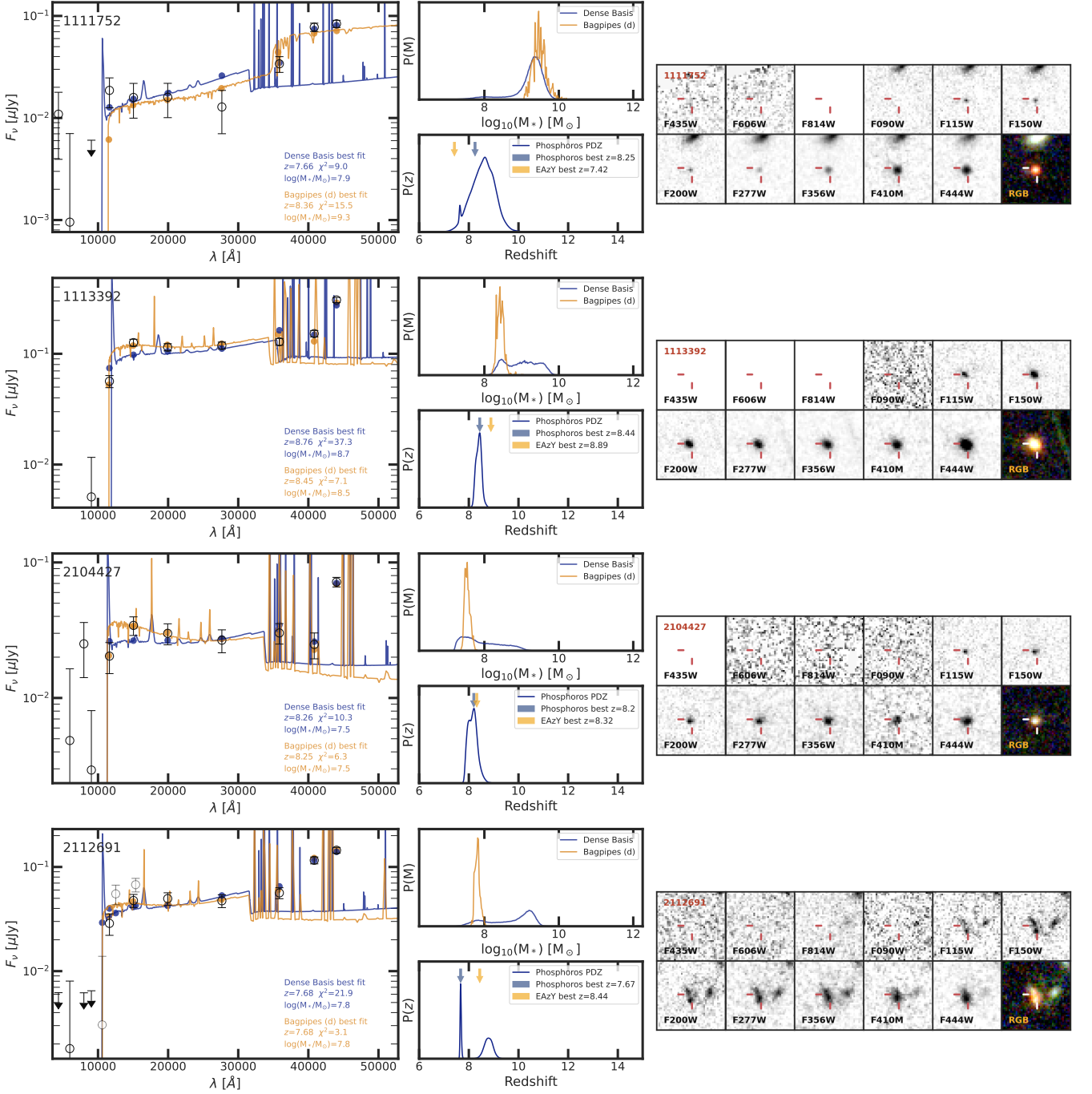


Figure A2. Observed photometry, SEDs fits, and image stamps for CANUCS double-break sources. For each source, the best model fits of both Dense Basis (blue) and Bagpipes (orange) are displayed, as well as the stellar mass posterior. In the case of Bagpipes, only the best fit configuration (noted a, b, c, d, or e) is displayed. The redshift sub-panels show for each source the Phosphoros $P(z)$ (blue curve), and the arrows indicate the Phosphoros (blue) and EAZY (orange) best fit redshifts. The stamps show the sources in the *HST* optical bands and in all the observed *JWST* bands, and the RGB stamps are using respectively a combination of F444W+F410M+F356W, F356W+F277W+F200W, and F150W+F115W+F090W for sources in *CLU* fields and F444W+F410M+F360M+F335M+F300M, F300M+F277W+F250M+F210M+F182M, and F162M+F150W+F140M+F115W+F090W for sources in the *NCF* fields.

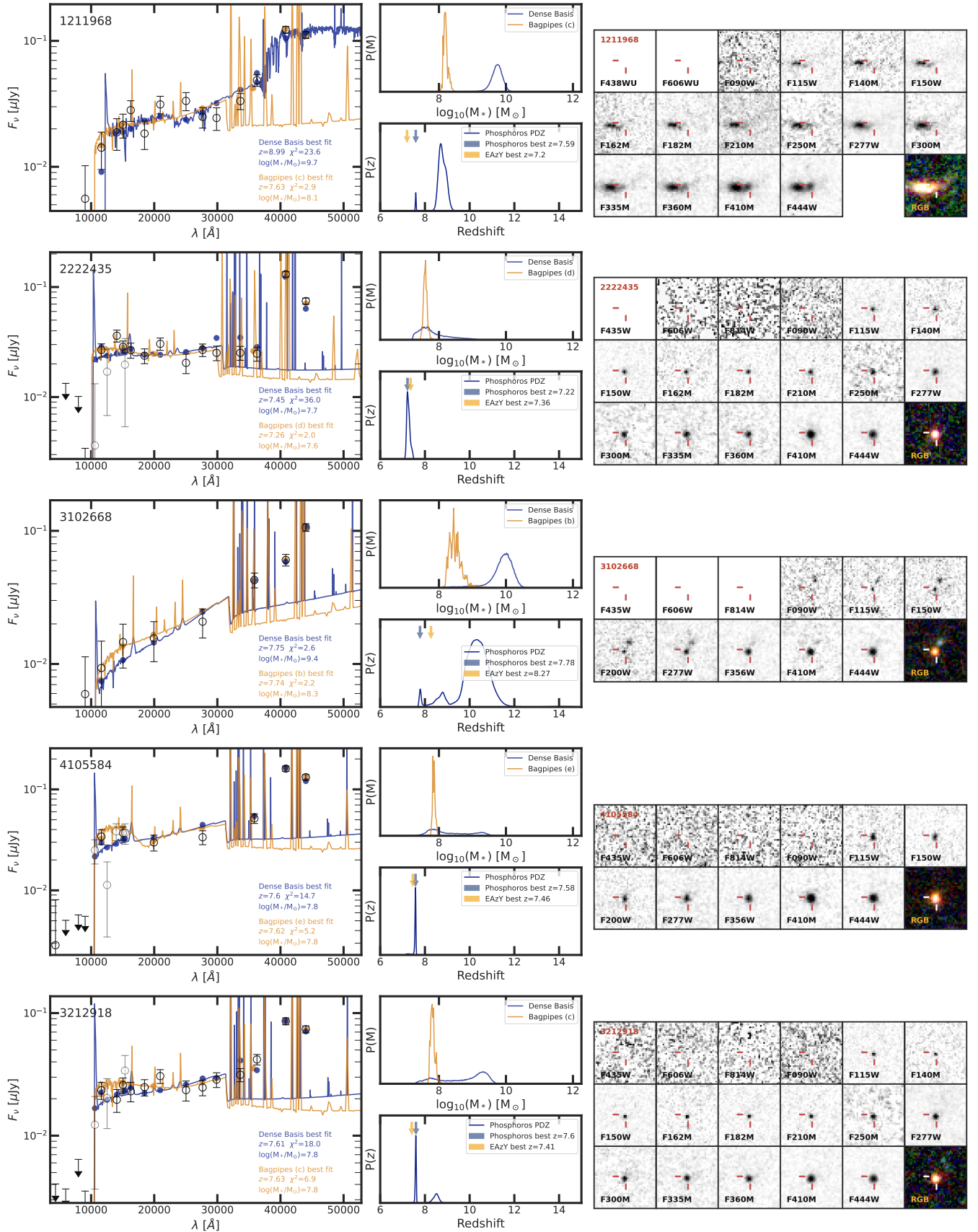


Figure A3. Same as Figure A2.

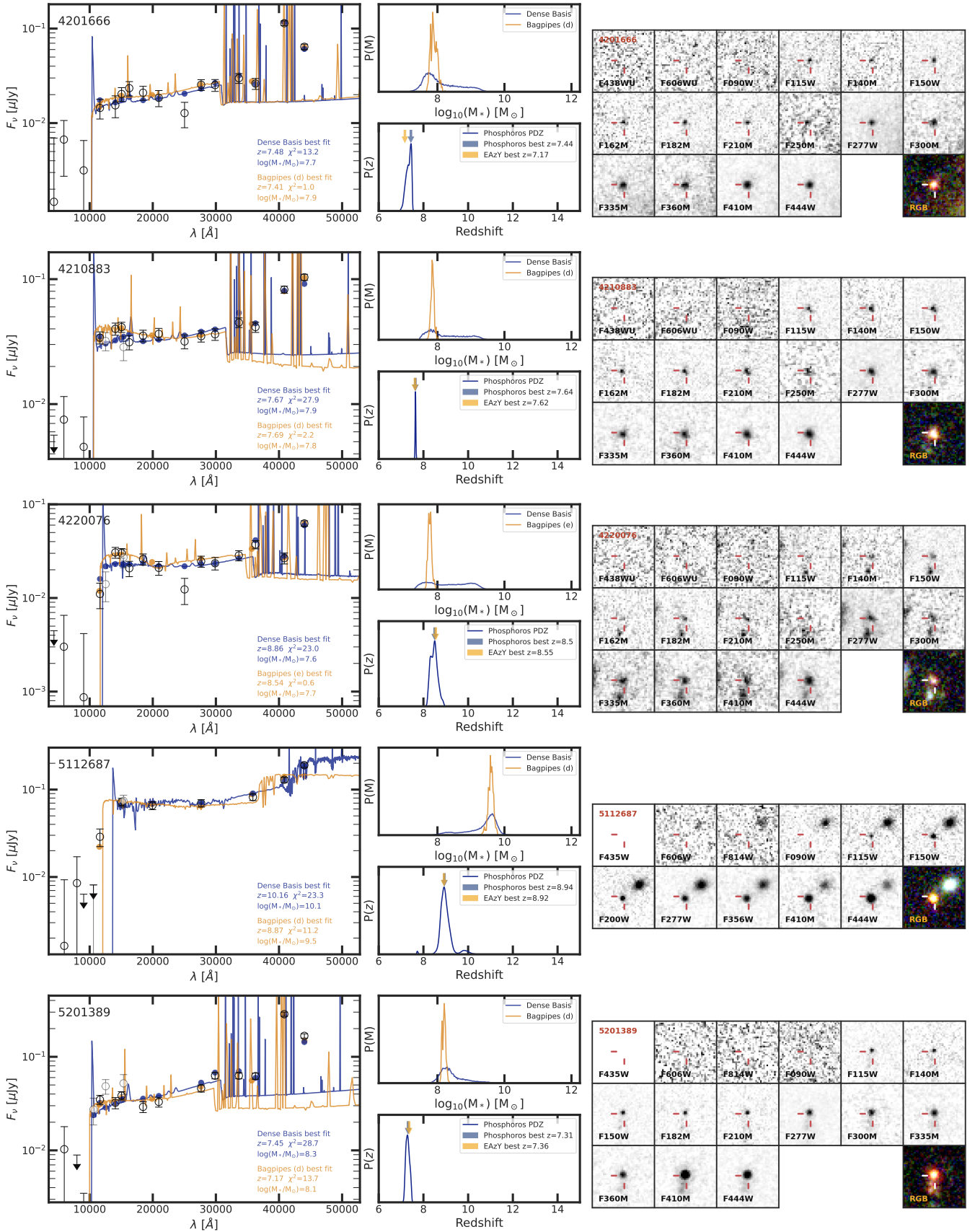


Figure A4. Same as Figure A2.

Table A2. List of 3σ magnitude depths reached in each field in $0''.3$ circular apertures for all available filters. *HST*/ACS values marked with an asterisk are actually *HST*/WFC3/UVIS data, where F435W row presents the UVIS/F438W band depth and the F606W row shows the UVIS/F606W one.

Band	MACS 0417		Abell 370		MACS 0416		MACS 1423		MACS 1149	
	<i>CLU</i>	<i>NCF</i>	<i>CLU</i>	<i>NCF</i>	<i>CLU</i>	<i>NCF</i>	<i>CLU</i>	<i>NCF</i>	<i>CLU</i>	<i>NCF</i>
F090W	29.1	29.7	29.5	29.9	29.3	29.8	29.3	29.8	29.4	30.0
F115W	29.4	29.7	29.5	29.9	29.3	29.8	29.3	29.8	29.4	29.9
F140M	—	29.0	—	29.2	—	29.2	—	29.2	—	29.1
F150W	29.4	30.0	29.6	30.1	29.5	30.0	29.6	30.1	29.6	30.3
F162M	—	29.1	—	29.3	—	29.2	—	29.3	—	—
F182M	—	29.8	—	29.9	—	29.8	—	29.8	—	29.8
F200W	29.5	—	29.7	—	29.7	—	29.8	—	29.7	—
F210M	—	29.5	—	29.7	—	29.7	—	29.7	—	29.7
F250M	—	29.0	—	29.2	—	29.2	—	29.3	—	—
F277W	29.8	30.4	30.2	30.6	30.2	30.6	30.2	30.7	30.2	30.8
F300M	—	29.4	—	29.6	—	29.7	—	29.7	—	29.6
F335M	—	29.8	—	29.9	—	29.9	—	30.0	—	30.1
F356W	30.0	—	30.2	—	30.2	—	30.3	—	30.2	—
F360M	—	29.9	—	29.9	—	29.9	—	30.0	—	29.9
F410M	29.1	29.8	29.5	29.9	29.5	29.9	29.6	29.9	29.5	29.9
F444W	29.6	30.0	29.7	30.1	29.7	30.2	29.8	30.2	29.7	30.1
F435W	29.3	28.6*	30.0	30.1	30.2	30.2	29.4	28.5*	29.8	30.2
F606W	29.7	29.3*	30.0	30.2	30.4	29.9	29.8	29.2*	30.2	30.2
F814W	28.2	—	30.3	30.2	30.5	30.4	29.0	—	30.3	30.3
F105W	28.0	—	30.0	30.2	30.1	30.3	28.7	—	30.2	30.2
F125W	27.2	—	29.5	29.6	29.8	29.8	28.5	28.3	30.0	29.8
F140W	27.2	—	29.3	29.6	29.7	30.0	28.4	—	29.5	29.6
F160W	27.7	—	29.5	29.7	29.7	29.9	28.4	28.1	29.8	29.6